Kinetic Control in Assembly of Plasmid DNA/Polycation Complex Nanoparticles

Yizong Hu[†,‡], **Zhiyu He**[‡,§], **Yue Hao**[¶], **Heng-wen Liu**[‡,§], **Like Gong**[‡,§], **Gregory Howard**[†,‡], **Hye-Hyun Ahn**[¤], **Mary Brummet**[¤], **Xiyu Ke**[‡,§], **Caleb Anderson**[‡,#], **Jung-Hee Seo**[¶], **Jinchang Zhu**[‡,§], **Kuntao Chen**[‡,§], **Marion Pang Wan Rion**[†,‡], **Honggang Cui**[‡,#], **Christopher G. Ullman**[^], **Christine A. Carrington**[^], **Martin G. Pomper**[¤,‡], **Rajat Mittal**[¶], **Il Minn**[¤,‡], **Hai-Quan Mao**[*,†,‡,‡,§]

[†]Department of Biomedical Engineering, Johns Hopkins University School of Medicine, Baltimore, MD 21287, USA.

[¤]Russell H. Morgan Department of Radiology and Radiological Science, Johns Hopkins University School of Medicine, Baltimore, MD 21287, USA.

[‡]Translational Tissue Engineering Center, Johns Hopkins University School of Medicine, Baltimore, MD 21287, USA.

[‡]Institute for NanoBioTechnology, Johns Hopkins University, Baltimore, MD 21218, USA.

[§]Department of Materials Science and Engineering, Johns Hopkins University, Baltimore, MD 21218, USA.

[¶]Department of Mechanical Engineering, Johns Hopkins University, Baltimore, MD 21218, USA.

[*]Correspondence should be addressed to Dr. Hai-Quan Mao: 3400 N. Charles Street, Croft Hall 100, Institute for NanoBioTechnology, Johns Hopkins University, Baltimore, MD, 21218, USA. hmao@jhu.edu.

#Department of Chemical and Biomolecular Engineering, Johns Hopkins University, Baltimore, MD 21218, USA.

^Cancer Targeting Systems, Chesterford Research Park, Cambridge, CB10 1XL, UK.

Abstract

Polyelectrolyte complex (PEC) nanoparticles assembled from plasmid DNA (pDNA) and polycations such as linear polyethyleneimine (lPEI) represent a major non-viral delivery vehicle for gene therapy tested thus far. Efforts to control the size, shape and surface properties of pDNA/polycation nanoparticles have been primarily focused on fine-tuning the molecular structures of the polycationic carriers and on assembly conditions such as medium polarity, pH, and temperature. However, reproducible production of these nanoparticles hinges on the ability to control the assembly kinetics, given the non-equilibrium nature of the assembly process and nanoparticle composition. Here we adopt a kinetically controlled mixing process, termed flash nanocomplexation (FNC), that accelerates the mixing of pDNA solution with polycation lPEI solution to match the PEC assembly kinetics through turbulent mixing in a microchamber. This achieves explicit control of the kinetic conditions for pDNA/lPEI nanoparticle assembly as demonstrated by the tunability of nanoparticle size, composition, and pDNA payload. Using a combined experimental and simulation approach, we prepared pDNA/lPEI nanoparticles having an average of 1.3 to 21.8 copies of pDNA per nanoparticle and average size of 35 to 130 nm in a more uniform and scalable manner than bulk mixing methods. Using these nanoparticles with well-defined compositions and sizes, we showed the correlation of pDNA payload and nanoparticle formulation composition with the transfection efficiencies *in vitro* and *in vivo*. These nanoparticles exhibited long-term stability at −20°C for at least 9 months in a lyophilized formulation, validating scalable manufacture of an off-the-shelf nanoparticle product with well-defined characteristics as a gene medicine.

Keywords

gene delivery; DNA/polycation nanoparticle; polyelectrolyte complex; kinetic control; turbulent mixing; linear polyethyleneimine; transfection

---

Polyelectrolyte complex (PEC) formation has been widely used to assemble particulate vehicles for delivery of a wide range of macromolecular therapeutics including plasmid DNA (pDNA), messenger RNA (mRNA), small interfering RNA (siRNA), proteins, and peptides. As a promising non-viral gene delivery approach, pDNA molecules are condensed and packaged into PEC nanoparticles using a polycationic carrier in an aqueous solution. The assembled pDNA/polycation nanoparticles facilitate transport and access to target cells and cellular compartments, and protect pDNA from enzymatic degradation.[1] The *in vivo* fate and delivery efficiency of the nanoparticles, as revealed by many recent works, are dependent on nanoparticle characteristics such as size range and distribution,[2] morphology,[3] surface properties, composition, and structure.[4] However, it has been challenging to determine a detailed understanding of the relationship between the characteristics of nanoparticles and their interactions with biological systems. This is largely due to the lack of

sufficient control over the PEC assembly kinetics that dictates the characteristics of the assembled nanoparticles.

The polymeric nature of the assembly components, for example, pDNA as the polyanion and lPEI as the polycation, indicates slower diffusion rates of these chains comparing with their electrostatic complexation rate. As a result, the PEC assembly often yields non-equilibrium, kinetically arrested complex structures. During the assembly process, the transient and local concentration profiles of different components determine how each PEC assembly initiates, propagates, and terminates to form a distinct nanoparticle. Control over these kinetic conditions is only possible when mixing is faster than the assembly process to allow distribution of the assembly components in a homogenous manner before each nanoparticle starts to assemble. Homogeneous mixing not only ensures that PEC nanoparticles are produced with uniform characteristics, but also provides the opportunity to control the size, surface properties, and composition of the nanoparticles through manipulation of the parameters of the inputs that go into the assembly system. Such an assembly condition implies that the characteristic mixing time (τ_M), within which different assembly components are mixed homogenously, must be reduced to less than the characteristic assembly time (τ_A), over which the PEC nanoparticle assembly occurs. The conventional mixing methods, such as pipetting and vortexing, cannot fulfill this requirement.

Mixing occurs through diffusion of assembly components across the interfaces of different flows. The most common approach to achieve small τ_M is by shortening the diffusion path. This can be achieved by both laminar flow and turbulent flow set-ups. In a laminar flow set-up, mixing is achieved as different flow paths are introduced within a small compartment. Due to manufacturing difficulties, engineering approaches such as hydrodynamic focusing[5–6] and droplet confinement[7] have been developed to further increase surface-to-volume ratio. In a turbulent flow set-up, turbulent eddies enable rapid flow break-down to tiny dimensions to facilitate diffusion. Flow turbulence can be delivered by T connectors,[8] Tesla mixers and herring-bone mixers,[9] coaxial jet mixers,[10–11] confined impinging jets (CIJ),[12–13] and multi-inlet vortex mixers (MIVM).[14–16] Various degrees of success have been achieved using these devices to prepare drug-loaded nanoparticles with more uniform characteristics compared to those produced with conventional methods, owing to a higher degree of control of mixing kinetics of the assembly components. We recently reported the production of pDNA/lPEI nanoparticles by turbulent mixing in a CIJ mixer to demonstrate the scalability of the method and feasibility of controlling the size,[17] but the kinetics of mixing and nanoparticle assembly during this process has not been fully analyzed.

Kinetically restricted assembly has been well illustrated for self-assembly of amphiphilic polymeric micelles where nanoparticle formation can be tuned by changing solvent mixing rate *vs.* polymer aggregation and drug partition rates in mixed solvents in a process called flash nanoprecipitation (FNP).[18] FNP uses turbulent mixing in an MIVM or CIJ mixer to mix two opposing jets carrying miscible solvents in a time shorter than the characteristic time for hydrophobic chain aggregation. Uniform nanoparticles can be produced as a result of homogenous super-saturation conditions.[19–20] By varying kinetic conditions under such mixing status, a diffusion-limited and fusion-dominated aggregation mechanism for nanoparticle formation[21] and a quantitative model for predicting nanoparticle size have been

proposed.[22] Here we adopt a similar analysis to uncover the kinetic control aspects of pDNA/polycation PEC nanoparticle assembly.

In this work, we demonstrate the kinetic control of PEC assembly and nanoparticle formation using a turbulent mixing approach in a CIJ mixer, which is termed flash nanocomplexation (FNC). The diffusion kinetics of polyelectrolytes pDNA and linear polyethyleneimine (lPEI) in FNC is significantly different from that of the solvent and polymer in FNP, as the complexation kinetics mediated by polyelectrolyte charge neutralization is faster than hydrophobic aggregation of the polymer chain segments in FNP, and the PEC occurs in aqueous medium absent of organic solvent mixing that occurs in FNP. These factors contribute to the unique process and additional challenges for kinetic control of PEC assembly into nanoparticles in FNC. For this study, we selected *in vivo*-jetPEI® as the testing carrier due to its high transfection efficiency *in vivo* as the benchmark for non-viral carriers, its availability in GMP quality, and its molecular simplicity as a polycation with uniform charge density. Using PEC nanoparticles of *in vivo*-jetPEI® and plasmids of typical sizes of 4 to 7 kb as a model system, we examined the mixing flow regimen in a CIJ mixer using fluid dynamic simulations and analyzed the requirements of achieving kinetic control over the PEC assembly process. We demonstrated exquisite control over the pDNA/ *in vivo*-jetPEI® nanoparticle composition through manipulation of kinetic conditions, and characterized the effect of nanoparticle size and composition on their transfection efficiency *in vitro* and *in vivo*. We also analyzed the advantages of pDNA/*in vivo*-jetPEI® nanoparticles assembled under kinetically controlled conditions in terms of their transfection efficiency and translational potentials for non-viral gene therapy.

RESULTS AND DISCUSSIONS

Control of τ_M by turbulent mixing in CIJ and mixing theory of pDNA/lPEI system.

In the FNC setup used for this study and our previous paper,[17] two opposing flows with the same flow rate carrying pDNA and lPEI solutions, respectively, impinge in a CIJ microchamber with a volume of 27 μL that breaks down the two flows into turbulent structures at an appropriate flow rate (Q). These turbulent structures can be described using an average dimensional scale denoted as the Kolmogorov length scale η,[23] that is determined by the volume-averaged turbulent energy dissipation rate $\overline{\mathscr{E}}$:

$$\eta = \left(\frac{\upsilon^3}{\overline{\varepsilon}}\right)^{\frac{1}{4}} = \left(\frac{\upsilon^3}{\overline{f(Q, \overrightarrow{X})}}\right)^{\frac{1}{4}} \tag{1}$$

where $\overrightarrow{X}$ is spatial coordinates within the microchamber, and υ is the average kinematic viscosity of solution mixture in the efflux. Since it is difficult to determine $\overline{\mathscr{E}}$ experimentally, we adopted a simulation approach to obtain the distribution of $\varepsilon = f(Q, \overrightarrow{X})$ throughout the microchamber with regard to each flow rate input, and then calculate the $\overline{\mathscr{E}}$. Instead of approximating ε through dividing energy input by the mass over which the energy is dissipated as in a previous work on the CIJ device,[12] we generated a numeric solution of ε using a finite-difference method (see Experimental Section),[24–25] based on the mass and

momentum conservation functions of viscous fluids, the Navier-Stokes equations, and the actual CIJ device dimensions.

The simulation results are demonstrated by the instantaneous velocity isosurface and Q-criterion vortex isosurface distributions sampled at a representative time point $t = 110$ ms upon impinging, and the time-averaged turbulent kinetic energy (TKE) distribution profiles for $Q = 1$, 10 and 20 mL/min as shown in Fig. 1A. It shows a clear transition from a laminar mixing pattern to a turbulent mixing pattern that occurs around a flow rate of 10 mL/min. With a flow rate of 20 mL/min representing a condition for turbulent mixing, the two jet flows changed their direction upon impinging by 90° to move radially in parallel that formed a disk-like structure of the velocity isosurface (Fig. 1A–2 and Video S1). During this parallel movement, oscillations occurred due to intrinsic flow instability and caused twisting and deformation of the flows. On the periphery of the disk-like structure, the velocity isosurface broke apart and vorticial structures were shed that broke the flows into the turbulent mixing flow structures (Fig. 1A–3 and Video S2). The turbulent flow structures are illustrated in a simplified model shown in Fig. 1B–1, in which the pDNA and lPEI solution flows are separated on a scale of the Kolmogorov length η (Fig. 1B–2).

Mixing occurs as molecular diffusion across the interfaces between the pDNA and lPEI flows in the turbulent structures. The diffusion is asymmetric for the two species. The dimensions of a pDNA are much larger with a molecular weight on an order of millions of Dalton. Due to steric restrictions imposed by the double-helix structure, they assume a rod shape in aqueous solutions with a low ionic strength, decreasing their diffusivity to a magnitude of 10^{-8} cm^2/s in the solution.[26] The charged lPEI molecules in an aqueous solution at pH 3.5 (kept consistent in this study) with a molecular weight of 22 kDa have a diffusivity estimated to be about 10^{-5} cm^2/s,[26] which is 3 orders of magnitude higher than that of pDNAs. Therefore, the diffusion distance for a pDNA is approximately $30(\sim\sqrt{10^3})$ times shorter than that of a lPEI molecule within the same period of time. Therefore, we approximated the time scale for the mixing process of this pDNA/PEI system, *i.e.* the characteristic mixing time τ_M, as the diffusion time for an **lPEI molecule** to cross half of the Kolmogorov length scale η (Fig. 1B–2,3,4):

$$\tau_M = \frac{\left(\frac{1}{2}\eta\right)^2}{D_{l\text{PEI}}} \tag{2}$$

where $D_{l\text{PEI}}$ is the diffusion coefficient of lPEI molecules in the solution mixture.

These analyses showed that a higher mixing efficiency can be achieved by a smaller η as a result of greater turbulence generated by higher flow rate Q. Using this simulation framework, we quantitatively analyzed the relationship between τ_M and Q, and identified a powered $\tau_M \sim Q$ relationship (Fig. 1C) as shown in Eqs. 3 and 4, which was used to calculate all corresponding τ_M values for Q inputs for the CIJ device used in this study.

$$[\tau_M, \mathrm{ms}] = 1.266 \times 10^3 \times [Q, \mathrm{mL/min}]^{-1.478}$$
$$for\ the\ turbulent\ mixing\ region(Q \geq 10\ mL/min)$$

(3)

$$[\tau_M, \mathrm{ms}] = 4.292 \times 10^5 \times [Q, \mathrm{mL/min}]^{-3.909}$$
$$for\ the\ laminar\ mixing\ region(Q < 10\ mL/min)$$

(4)

Effect of characteristic mixing time τ_M on the outcomes for pDNA//IPEI nanoparticle assembly.

Next, we experimentally examined the effect of flow rate Q on FNC assembly of pDNA/IPEI nanoparticles when impinging gWiz-Luc pDNA (6.7 kb) solution and *in vivo*-jetPEI® solution. The following parameters were maintained constant for this study: the pH of the IPEI solution was kept consistent at 3.5 to maintain the same protonation degree of IPEI at around 75%, and thus the same charge density for IPEI,[27] and the concentrations of the input pDNA and *in vivo*-jetPEI® solutions were maintained at 200 µg/mL and 106 µg/mL, respectively. When increasing Q, *i.e.* decreasing τ_M, the size (z-average hydrodynamic diameter, D_Z) given by dynamic light scattering (DLS) measurement of the nanoparticles decreased until it reached a plateau of 65 nm at $Q\sim$15 mL/min (Fig. 2A).

When the concentrations of pDNA and IPEI were both proportionally reduced by 4-fold, or the pDNA size reduced from 6.7 to 4.4 kb (I2 plasmid, see Table S1), the measured DLS nanoparticle sizes followed the same trend. The critical Q above which consistent DLS size for the nanoparticles was obtained was lowered from ~ 15 to ~ 8.5 mL/min (critical $\tau_{M,0}$ increased from ~ 20 to ~ 85 ms) by the lowered input pDNA concentration. The DLS size standard deviation (a reflection of peak width, as defined in Experimental Section) of the nanoparticles showed the same dependency on Q (Fig. 2B), indicating increased uniformity of the nanoparticles as τ_M decreases. The flow rate-dependent average size and uniformity were confirmed by transmission electron microscopy (TEM) observations (Fig. 2C). Based on these findings, we could divide the field of characteristic mixing time τ_M or flow rate Q into two regions:

Region I corresponds to the kinetic condition where the average DLS size and uniformity remained constant independent of Q or τ_M. This indicates that the mixing conditions within the microchamber have reached the maximum degree of homogeneity to allow the assembly to occur uniformly, so that all nanoparticles have a similar assembly path. This assembly process has a time scale defined as the characteristic assembly time (τ_A), and with $\tau_M < \tau_A$, almost all pDNA/IPEI nanoparticles are assembled under the same defined conditions (concentrations of pDNA and IPEI, temperature, medium pH, ionic strength, etc.). In other words, the assembly components pDNA and IPEI can be mixed at a rate that is faster than nanoparticle formation to initiate nanoparticle assembly nearly "simultaneously" and in nearly the same microenvironment. As discussed above, $D_{I\mathrm{PEI}} \gg D_{\mathrm{DNA}}$, and it is IPEI molecules that primarily diffuse into pDNA flow regions, resulting in homogeneous distribution of IPEI molecules to the vicinity of pDNA molecules. This establishes uniform

initial kinetic conditions defined by the input concentration profiles of pDNA and lPEI (Fig. 1B–4).

Region II corresponds to the kinetic condition where $\tau_M > \tau_A$ such that the molecular mixing process occurs on a time scale that is greater than the nanoparticle assembly process. Under this condition, nanoparticle assembly happens in a heterogeneous manner as mixing progresses, and partially formed nanoparticles can further associate with late-arrival molecules in a poorly defined manner. This leads to less uniform and larger nanoparticle sizes, or even aggregates; and compositions of the nanoparticles are dependent on the flow rate and mixing condition. As the flow rate increases and approaches the critical condition allowing $\tau_M = \tau_A$, the assembly mixture is closer to turbulent mixing structure (Fig. 1A,B), and is becoming more homogenous. Therefore, the mixture composition becomes closer to the input concentration profiles of pDNA and lPEI. For example, when comparing Preparation 1 ($Q = 1.25$ mL/min and $\tau_M = 1.8 \times 10^5$ ms, based on Fig. 1C and Eq. 4), Preparation 2 ($Q = 5$ mL/min and $\tau_M = 7.9 \times 10^2$ ms, Eq. 4), and Preparation 3 ($Q = 20$ mL/min and $\tau_M = 15$ ms, Eq. 3), the nanoparticle ensembles showed the characteristics consistent with this analysis (Fig. 2A,C).

As the flow rate increases, *i.e.* as τ_M decreases, the flow mixing profile undergoes a transition from the laminar to turbulent mixing, which coincides with the nanoparticle assembly transition from Region II ($\tau_M > \tau_A$) to Region I ($\tau_M < \tau_A$). This shows the capability of turbulent mixing in a CIJ device to match the solution mixing time scale with the pDNA/lPEI nanoparticle assembly time scale by varying the flow rates from 1 to 50 mL/min.

Effect of pDNA concentration and N/P ratio on pDNA/lPEI nanoparticle assembly.

When assembly occurs under the kinetic conditions defined in Region I, the assembly concentration profiles of pDNA and lPEI are defined by the input concentrations (*i.e. p*DNA concentrations and N/P ratio in the impinging solutions). This provides an opportunity to examine the effect of assembly concentration profiles on nanoparticle characteristics. We selected a flow rate of 20 mL/min ($\tau_M = 15$ ms, as labeled in Fig. 2A,B) for this comparison. As shown in Fig. 2D, an increase in pDNA concentration resulted in increase of nanoparticle size, relatively narrow size distribution and low PDI (0.12 – 0.16) of these formulations (Fig. S1A,B). TEM observations (Fig. S2A) confirmed the kinetically controlled mixing and uniform assembly of the pDNA/lPEI nanoparticles. On the other hand, when the input pDNA concentration was fixed at 400 μg/mL, nanoparticles assembled at different ratios of nitrogen (in lPEI) to phosphorous (in pDNA) (N/P) gave similar size (Fig. 2F and Fig. S2B), indicating that the plasmid was compacted most effectively under this mixing condition independent of the initial lPEI concentration, and to a maximum compaction degree even when the N/P ratio was reduced to 3. This observation further confirms the effectiveness of the turbulent mixing with $\tau_M < \tau_A$ in maximizing the access of lPEI molecules to complex with pDNA during the assembly process. In addition, zeta-potential assessments revealed a similar surface charge around +40 mV for all formulations regardless of the plasmid used, or input pDNA concentration (Fig. 2E) or N/P ratio (Fig. 2G). This suggests that the nanoparticle surfaces are similar and consist of excess amount of lPEI molecules.

Conventional mixing methods for preparation of pDNA/polycation nanoparticles, such as pipetting, provide a mixing time on an order of seconds, therefore falling into **Region II** on this kinetics scale. The method of pipetting followed by vortexing (Table S2) using small volumes of solutions generated nanoparticles with average sizes and uniformity that are similar to those of FNC preparations with a flow rate $Q < 1.5$ mL/min. There was no clear dependence of the nanoparticle size on input pDNA concentration (Fig. S3). Moreover, there was a higher degree of variability in size (Fig. S3) as a result of different pipetting procedures (Table S2).

Average nanoparticle composition and free *l*PEI measurement.

Full complexation of pDNA by *l*PEI is achieved with an N/P ratio greater than 3; therefore, assembly with an N/P 3 would result in an excess of unbound or free *l*PEI in the nanoparticle suspension.[28] To assess the actual composition of the assembled nanoparticles, we first characterized the amount of free *l*PEI according to a published protocol.[29] When the pDNA/*l*PEI nanoparticles were assembled under the turbulent mixing condition ($Q = 20$ mL/min and $\tau_M = 15$ ms) as defined in Fig. 2, all nanoparticle formulations with different pDNA concentration inputs had the same bound *vs.* free *l*PEI compositions, as long as the input N/P ratio was fixed at 4 (Fig. 3A). The amount of bound *l*PEI was in the region of 70%, which corresponded to an N/P ratio of 2.7 in the nanoparticles. When adjusting the input N/P from 3 to 6 with a consistent pDNA concentration (Fig. 3B left panel), the amount of *l*PEI bound to nanoparticles was consistent regardless of the input N/P ratio. This indicates that the amount of *l*PEI bound to pDNA was the same among the nanoparticles prepared under different preparation conditions; and this average composition corresponds to an N/P ratio of 2.74 ± 0.14 (average $\pm$ standard deviation in $n = 28$ individual preparations with different input pDNA concentrations and/or N/P ratios) in the nanoparticles. These resultant "overcharging" nanoparticles are consistent with the fact that not all charged groups are accessible to participate in charge neutralization in the process of PEC formation.[30]

There was a minor difference between the two plasmids tested in that gWiz-Luc seemed to result in slightly lower amount of bound *l*PEI as N/P ratio decreased. Nonetheless, the overall conclusion is clear that the binding of *l*PEI to pDNA to form PEC is not affected by the concentrations of either pDNA or *l*PEI, nor by the input N/P ratio.

Charge neutralization is not a rate-limiting step for PEC nanoparticle assembly.

We found that this consistent minimal bound N/P ratio for pDNA neutralization was also true for nanoparticles prepared under non-turbulent mixing conditions (Fig. 3B right panel and Fig. 3C). The surface charges (*i.e.* zeta-potentials) measured for nanoparticles prepared under different mixing conditions also remained the same (Fig. 3C). Since *l*PEI content in the nanoparticles and zeta-potential are directly related to the charge neutralization and complex formation processes, our findings, highlighted in Fig. 3A–C, suggest that the charge neutralization and pDNA-*l*PEI binding are not rate limiting steps for nanoparticle assembly. In other words, charge neutralization occurs at a rate much faster than condensation and chain folding of the pDNA/*l*PEI PECs into nanoparticles, *i.e.* it occurs on a time scale that is much shorter than the total characteristic assembly time τ_A.

We then could model the pDNA/lPEI PEC nanoparticle assembly process achieved under kinetically controlled mixing conditions into two distinct steps, which is also in agreement with several literature reports:[31–32] **Step 1**: Charge neutralization step, in which lPEI molecules bind to the pDNA as soon as they diffuse into the vicinity of pDNA molecules forming pDNA/lPEI PECs, is not rate-limiting. In this study, regardless of input pDNA concentrations or N/P ratios, lPEI complexed with pDNA consistently at an N/P ratio of ~ 2.7. **Step 2**: PEC chain assembly, where the neutralized pDNA/lPEI complexes undergo condensation or compaction through folding[33–34] that significantly reduces the complex volume, occurs. This is the rate limiting step, such that the time scale for Step 2 is much larger than that of Step 1. Therefore, the characteristic assembly time τ_A is primarily determined by the completion time of Step 2. When the neighboring pDNAs or PECs are close enough to diffuse into each other during the assembly process before the structure is stabilized by repulsion from net positively surface charges, compaction and assembly involving multiple PECs could occur, resulting in multiple pDNAs being packaged into a single distinct nanoparticle.

Characterization of the average pDNA copy number in each pDNA/lPEI nanoparticle.

Given that we have prepared nanoparticles with narrow size distribution and consistent composition, we aimed at characterizing the molar mass of the nanoparticles using the static light scattering (SLS) technique. With a fixed in-nanoparticle pDNA/lPEI mass ratio (Fig. 3A), we assumed that the refractive increment (dn/dc) value of the nanoparticles is constant and follows the additive rule.[35] By measuring the intensity of scattered light to obtain Rayleigh scattering ratio with regard to each scattering angle and each nanoparticle mass concentration, and extrapolating concentration and angle-dependence curves to zero concentration and zero angle on a Zimm plot, we can characterize the weight average molar mass of nanoparticles $\overline{M}_{w, Nanoparticle}$, from which the weight average copy number of pDNA per nanoparticle ($\overline{N}$) can be calculated (see Experimental Section).[36–37] A representative Zimm plot for pDNA/lPEI nanoparticles with an $\overline{N} = 13.5$ is shown in Fig. 3D. For all nanoparticles measured by this method (Fig. 3D and Fig. S5A,B,C), the Zimm plot analyses indicate that the second virial coefficient (A_2) of these nanoparticles approaches zero. This finding implies that the solvent (water) and temperature (25°C) conditions used for SLS measurement satisfies the θ condition, $i.e.$ the PEC-solvent interaction cancels out the Vander Waals interaction and volume expansion of the PEC chains such that the PEC chain compaction occurs in a random packing manner. This θ condition significantly simplifies the measurement of average molar mass since we could ignore the concentration dependence of the light scattering behavior of these nanoparticles and measure the Rayleigh ratios at a fixed concentration, and apply calculations using the Debye plots (Fig. 3E and Fig. S5D,E,F). We found that $\overline{N}$ for pDNA/lPEI nanoparticles prepared under a turbulent mixing condition ($Q = 20$ mL/min) varied significantly depending on the input pDNA concentrations: 1.3 to 13.5 for I2 pDNA (Fig. 3F); 1.6 to 10.0 for gWiz-GFP pDNA (Fig. 3F); and 1.4 to 21.8 for gWiz-Luc pDNA (Fig. 3G). On the other hand, varying input N/P ratio showed minor changes in the average number of plasmids in each nanoparticle. When input N/P ratio changed from 3 to 6 for input of 400 µg/mL pDNA,

$\overline{N}$ decreased from 9.2 for N/P = 3 to 6.1 for N/P = 4, 5.0 for N/P=5, and 4.4 for N/P=6 (Fig. 3G and Fig. S5F).

Correlation of DLS size and molar mass of *p*DNA/*l*PEI nanoparticles.

When the measured weight average molar masses of nanoparticles prepared under different conditions for all three plasmids were plotted against their hydrodynamic volume dimensions (*i.e. $D_z{}^3$*) (Fig. 4A), a common linear correlation emerged:

$$\left[\overline{M}_{w,\,Nanoparticle}, \mathrm{Da}\right] = 67.7 \times \left[D_Z, \mathrm{nm}\right]^3 + 1.93 \times 10^6 \qquad (5)$$

where D_z is the z-average size as measured by DLS of the nanoparticle suspension, and $\overline{M}_w$ is the weight average molar mass of the nanoparticles given by SLS. Such a "universal" fit for various nanoparticles independent of the plasmid and conditions used for nanoparticle assembly suggest that the PEC assembly units and compaction degree of these nanoparticles are similar. More specifically, Eq. 5 suggests that these nanoparticles have the same apparent hydrodynamic density of 67.7 Da/nm^3, *i.e. p*DNAs are condensed to the same degree no matter how many of them are packed into a single nanoparticle.

Similarly, we also identified another composition-size correlation that the weight average molar mass of the nanoparticles is linearly proportional to the second power of radius of gyration (*i.e. $R_g{}^2$*) (Fig. 4B):

$$\left[\overline{M}_{Nanoparticle}, \mathrm{Da}\right] = 22,251 \times \left[R_g, \mathrm{nm}\right]^2 + 4.17 \times 10^6 \qquad (6)$$

This correlation fits well for nanoparticles with D_z between 50 and 130 nm, and the deviation from experimental data points increases as the size goes smaller than 50 nm. This linear relationship between $\overline{M}$ and $R_g{}^2$ further confirms that these *p*DNA/*l*PEI nanoparticles are assembled and characterized under the θ condition; and the PEC units assume random packing behavior under the solvent and temperature conditions tested.[37] If we consider each PEC chain formed in Step 1 (a *p*DNA with all its bound *l*PEI) as a packing unit (*i.e.* a PEC unit) for nanoparticle assembly in Step 2, a *p*DNA/PEI nanoparticle can be modeled as an entity consisted of either one or multiple PEC units. The nanoparticle assembly follows a quantized combination pattern.

Nanoparticles generated by N/Ps varying from 4 to 6 have a similar molar mass, while those generated by N/P = 3 are heavier in molar mass but still fall into the two linear fits of Eq. 5 and Eq. 6 (Fig. 4C). It is presumed that with input N/P larger than 2.7, where *l*PEI is in excess to the amount required to sufficiently compact *p*DNAs, quantized combination stays valid.

This model is further supported by the fact that nanoparticles prepared under laminar mixing condition ($\tau_M > \tau_A$) also follow the same correlation of Eq. 5 (Fig. 4D). It is remarkable that nanoparticles with lower uniformity (*i.e.* broader distribution) appeared to have the same apparent hydrodynamic density as that of more uniform nanoparticles with fewer copies of *p*DNA per nanoparticle. This analysis is consistent with the hypothesis that PEC units

formed in Step 1 are the building blocks for nanoparticle assembly, and they are compacted and associated in a similar manner as random folding of PEC unit chains in the solution under the θ condition.

Modeling *p*DNA/*l*PEI nanoparticle assembly kinetics in FNC under turbulent mixing condition.

Based on these findings and the nanoparticle assembly model mentioned above, we could analyze the assembly kinetics under $\tau_M < \tau_A$ condition to understand the concentration-dependent mechanism for determining *p*DNA copy number per nanoparticle (Fig. 4E). The rate of *p*DNA-*l*PEI binding (*i.e.* PEC unit formation) in Step 1 is much faster than the rate of PEC compaction and association in Step 2 (as a conclusion from Fig. 3A,B,C), such that $\tau_{Step\,1} \ll \tau_{Step\,2}$, and $\tau_A \cong \tau_{Step\,2}$. The characteristic assembly time τ_A is presumably influenced by intrinsic properties of the polyelectrolytes involved in nanoparticle assembly, such as plasmid length, *l*PEI structure and molecular weight, stoichiometric and steric nature of *p*DNA-*l*PEI binding, etc. Upon generation of the turbulent flow structures (defined as $t = 0$), mixing occurs primarily by *l*PEI molecules diffusing into the *p*DNA solution regions, and *l*PEI diffusion proceeds on a time course of τ_M. The fast *l*PEI binding onto *p*DNAs happens with an N/P ratio of ~ 2.7 as *l*PEIs diffuse. When t τ_M, mixing completes and results in almost all *p*DNAs bound with the same amount of *l*PEIs, forming uniform PEC units that are about to proceed to Step 2 as the building blocks for nanoparticle assembly. The assembly occurs under the θ condition (Fig. 3D, Fig. 4B, and Eq. 6), where PEC chain-chain interaction cancels the PEC-solvent interaction. There is no additional barrier for multi-PEC chain folding and association as opposed to single PEC chain folding. As a result, the compaction of PEC units ends with the same condensation degree regardless of the number of *p*DNA involved in the assembly of a single nanoparticle (*i.e.* regardless of the final $\overline{N}$). An $\overline{N} > 1$ is possible when multiple PEC units are brought into contact by diffusion for multi-PEC chains to be compacted into a single nanoparticle. Therefore, the number of PEC units that is involved in the assembly of a single nanoparticle is dictated primarily by PEC diffusion within the time course of τ_A. A higher input *p*DNA concentration results in a higher *p*DNA concentration in the *p*DNA flow regions in the turbulent flow structures, thus a lower average distance between *p*DNA molecules in the solution, such that more PEC units could be associated within a time scale similar to τ_A as a result of a shorter diffusion distance between them. Therefore, it is possible to explicitly control the number of *p*DNA to be packaged into a single nanoparticle under the kinetically controlled mixing conditions defined in the FNC process (*i.e.*, when $\tau_M < \tau_A$).

Based on the analysis above, if the input *p*DNA concentration is sufficiently low, such that the average distance between any two *p*DNA molecules is too large for them to diffuse into each other over the time scale of τ_A, single plasmid-containing nanoparticles can be produced. With the correlation of weight average molar mass and nanoparticle size (Fig. 4A), the extrapolated size limit when $c \rightarrow 0$ falls between 30 and 40 nm for the plasmids (4.4 kb to 6.7 kb) tested in this study (Fig. 2D), represents a typical size for *p*DNA/*l*PEI nanoparticles containing only one *p*DNA per nanoparticle. This small size and single-*p*DNA payload were never achieved by pipetting, for which mixing kinetics were poorly controlled, as shown in Fig. S3 with the lowest input pDNA concentration of 25 μg/mL.

Transfection efficiency of *p*DNA/*l*PEI nanoparticles with different copy numbers of *p*DNA per nanoparticle.

Using gWiz-Luc plasmid at different concentrations, we generated nanoparticles in our FNC device at a flow rate of 20 mL/min with $\overline{N} = 1.7$ (input $c = 100$ μg/mL), 3.5 (input $c = 200$ μg/mL), 6.1 (input $c = 400$ μg/mL) and 21.8 (input $c = 800$ μg/mL). With this series of nanoparticles, we examined the effect of $\overline{N}$ on the *in vitro* and *in vivo* transfection efficiency of these nanoparticles. It is important to note that the sizes of these nanoparticles are also different, even though surface charges (zeta potentials) and compositions (bound and free *l*PEI fractions) are the same (Table S4).

Previous reports demonstrate dependence of cellular uptake on nanoparticle size due to differences in surface contact, avidity and trafficking kinetics.[2] We used ^{3}H-labelled *p*DNA to assemble nanoparticles (see Experimental Section) with different $\overline{N}$ to assess their cellular uptake over a 4-h incubation period with PC3 prostate cancer cells. Our data showed no significant difference among these nanoparticle groups (Fig. 5A). As we fixed the total *p*DNA dose (0.6 μg per 1×10^4 cells with 5×10^4 per well in a 24-well plate) for the transfection test, the measured total fraction of nanoparticle uptake (out of the total dosed nanoparticles) is a function of the total number of nanoparticles available per cell and uptake rate. Presumably, a formulation with higher $\overline{N}$ has fewer nanoparticles in number and thus higher cellular uptake rate. *In vitro* transfection efficiency experiments in the PC3 cancer cell line showed that $\overline{N} = 6.1$ and 21.8 had similar transfection efficiency levels and that these were much higher than those of either $\overline{N} = 1.7$ or 3.5 (Fig. 5B). With the similar uptake *p*DNA amount for each time point considered, $\overline{N} = 6.1$ and 21.8 may have higher efficiencies in intracellular delivery process, such as endosomal escape, *p*DNA dissociation, and nuclear transport. In previous literature reports, *p*DNA/*l*PEI nanoparticles typically give transfection and transgene activity in the lung following intravenous (*i.v.*) injection.[38] Consistent with the *in vitro* findings, $\overline{N} = 1.7$ showed an appreciably lower transfection efficiency than other formulations, and there was a perceived trend for nanoparticles with $\overline{N} = 3.5$, 6.1, and 21.8 that a higher $\overline{N}$ gave better transfection efficiency (Fig. 5C and Fig. S7) *in vivo* in lungs of healthy BALB/c mice.

A biodistribution study was conducted in BALB/c mice by *i.v.* injection of ^{3}H-labeled nanoparticles at a dose of 30 μg *p*DNA/mouse. Mice were sacrificed at 1 h following dosing of the nanoparticles, and major organs and blood samples were collected and weighted. The biological samples were solubilized, and the solutions were subjected to liquid scintillation assessment to quantify ^{3}H-labeled *p*DNA in the samples. The results revealed a rapid distribution (> 95%) of the nanoparticles into organs and tissues within 1 h for all formulations. The distribution patterns of these nanoparticles were similar, except that those with an $\overline{N}$ of 1.7 resulted in fewer nanoparticles deposited in the lung (Fig. 5D and Fig. S8A) and the clearance *via* the spleen was more significant (Fig. S8C). For all groups, even though 42–45% of the total dose ended up in the liver, compared with 5–8% of the dose to the lung (Fig. S8B), there was no detectable level of transgene expression in the liver. This was probably due to the rapid clearance and degradation of nanoparticles by the Kupffer cells in the liver.[39]

The smaller difference in *in vivo* delivery efficiency among these nanoparticles was likely due to the fact that *p*DNA/*l*PEI nanoparticles interact strongly with serum components and aggregate rapidly following *i.v.* injection, leading to entrapment in the lung microvasculature and substantial uptake by endocytic cells in the liver and lung,[40] which would mask the differences of the payload capacity as a result of controlling $\overline{N}$. Identifying nanoparticles (*e.g.* PEGylated nanoparticles) with a lower tendency for opsonization and aggregation, and understanding the mechanism of serum coating will help to better reveal the detailed effects of nanoparticles with defined composition and size on transfection efficiency *in vivo*, as a future direction.

Effect of *p*DNA payload and the ratio of bound *vs.* free PEI content on the *in vitro* and *in vivo* transfection efficiency of *p*DNA/*l*PEI nanoparticles prepared under kinetically controlled conditions.

The pilot study described above revealed that nanoparticles with $\overline{N}$ of 6 or higher showed better transfection efficiency *in vitro* and *in vivo* than nanoparticles with lower plasmid payload. We next examined nanoparticles prepared under defined turbulent mixing conditions ($Q = 20$ mL/min, $\tau_M = 15$ ms $< \tau_A$) at different N/P ratios and compared them with those prepared by poorly mixed condition ($Q = 5$ mL/min, $\tau_M = 790$ ms $\gg \tau_A$). Two series of nanoparticles were prepared with gWiz-Luc plasmid, with characteristics shown in Table 1.

We first tested all nanoparticles prepared with gWiz-Luc plasmid in the PC3 cancer cell line (Fig. 6A). For the two sets of FNC nanoparticles (W1–W4 and W5–W8), a higher N/P ratio (*i.e.* a higher free PEI fraction as a result) yielded a higher transfection efficiency, which was in agreement with previous literature reports.[38, 41] Nanoparticles carrying lower payload showed a better performance than those nanoparticles with a higher payload; and the differences were statistically significant at N/P = 4 and 6. We then administered the same sets of nanoparticles to BALB/c mice and monitored their transfection efficiencies in the lung at 12, 24 and 48 h post-injection time points. The results (Fig. 6B and Fig. S10) showed a similar pattern to the *in vitro* experiments. Transgene expression activity was low for nanoparticles prepared at an N/P ratio of 3 for both low-payload and high-payload nanoparticles. With an N/P = 4, nanoparticles with a low payload ($\overline{N} = 6.1$) were more effective than nanoparticles with a higher payload ($\overline{N} = 45.6$). The transgene activities of the nanoparticles prepared at N/P = 5 and 6, regardless of the payload level, $\overline{N}$, showed similar luciferase expression levels to the N/P = 4, $\overline{N} = 6.1$ formulation.

We then sought to confirm these findings in an LL/2 lung metastasis model in NSG mice. Tumor-specific transfection and expression were investigated through preparations of *p*DNA/*l*PEI nanoparticles using a custom-built plasmid construct encoding luciferase gene driven by a tumor-specific PEG-3 promoter as we have reported previously.[42–43] We prepared the same set of nanoparticles (P1–P8) as described above under different assembly conditions using the FNC setup (Table 1). Tumor inoculation was conducted by injection of 200 μL PBS containing 5×10^5 LL/2 tumor cells into immunodeficient NSG mice 7 days prior to nanoparticle dosage. In this mouse model, tumor cells primarily engraft in the lung.[44] Mice with successful tumor engraftment in the lung were selected and randomly grouped

for this experiment. Mice were imaged at 48 h following nanoparticle injection by IVIS imaging. The tumor-specific gene expression in the lungs of the engrafted NSG mice showed a similar transgene expression pattern as that in healthy BALB/c mice transfected by gWiz-Luc plasmid (Fig. 6C and Fig. S11). Nanoparticles prepared with higher N/P ratios (4 to 6) showed higher transfection efficiencies than those prepared at N/P = 3, though the lower payload nanoparticles ($\overline{N}$ = 9.5) performed better than higher payload nanoparticles ($\overline{N}$ = 49.7) at N/P = 4. Transgene expression levels in the lung was comparable among nanoparticles with N/P = 5 or 6. There was a perceived trend (however $p > 0.05$) that for lower payload nanoparticles generated by a flow rate of 20 mL/min, higher N/P ratio resulted in greater average transgene expression level in the lung.

We also characterized the biodistribution of four selected nanoparticle formulations from this series with the biggest differences in their transfection efficiencies: nanoparticles with lower payload and lower N/P ratios (Table 1, W1: N/P = 3 and $\overline{N}$ = 9.1, W2: N/P = 4 and $\overline{N}$ = 6.1), and nanoparticles with higher payload and higher N/P ratios (Table 1, W6: N/P = 4 and $\overline{N}$ = 45.6, W8: N/P = 6 and $\overline{N}$ = 42.8). The ^{3}H-labeled nanoparticles were injected intravenously at the same dose as used for Fig. 6B in BALB/c mice. More than 95% of the injected nanoparticle dose was distributed to tissues and organs within 1 h (Fig. 6D). Compared with the other nanoparticle formulations, W1 nanoparticles had the lowest fraction of nanoparticles distributed into the lung (1.4%) (Fig. 6D,E) with the highest levels of distribution to the liver (54%, though with no statistical significance) and spleen (6%) (Fig. S12), correlating with the lowest transfection efficiency in the lung. W2 and W8 showed similar levels of distribution to the lung (Fig. 6D,E), which correlated with similar transgene expression levels in these two formulations (Fig. 6C). However, although W6 had a similar biodistribution profile to W2, it gave a significantly lower transfection efficiency. This may be attributed to less efficient intracellular delivery efficiency as shown in the *in vitro* study (Fig. 6A), plus delivery of 7.5-fold fewer nanoparticles to the lung. For lower payload nanoparticle formulations, the increased number of nanoparticles may facilitate more frequent transfection events in a higher number of cells. On the other hand, the smaller size of these nanoparticles may positively influence nanoparticle trafficking in the tissue and the access to tumor tissues. Comparing W6 and W8 nanoparticles, even though their payloads ($\overline{N}$ = 45.6 and 42.8) and sizes (D_Z = 158.9 and 155.5 nm) were similar, a higher level of free *l*PEI (Fig. 3B, 1.75 mM *vs.* 0.74 mM) led to a lower level of clearance by the liver (Fig. 6D and Fig. S12A). Together with a higher intracellular delivery efficiency (Fig. 6A), this factor may be responsible for a relatively higher transgene expression activity in the lung.

Scale-up production of an off-the-shelf, lyophilized *p*DNA/*l*PEI nanoparticles.

Successful clinical translation of non-viral DNA delivery gene therapy depends on a high delivery and transfection efficiency, good biocompatibility, scalable production processes, prolonged storage stability, and good performance consistency (*i.e.* low batch-to-batch variability). Current methods for systemic delivery of *p*DNA through PEC nanoparticles rely on on-site mixing of the therapeutic *p*DNA and *in vivo*-jetPEI® solutions in the clinic immediately before administration (i.e. a process that is essentially similar to manual pipetting, as W9 in Table 1). As could be expected, defining the reproducibility of

nanoparticle formation and performance consistency of such a process would be difficult (Fig. S2). The preparation of nanoparticles by the FNC process that we have reported here offers a continuous, and therefore highly scalable and reproducible method.[15–17] With a single bench-model device, 0.5 grams of *p*DNA, which is equivalent to 12,500 doses at 40 µg *p*DNA/mouse, could be packaged into *p*DNA/*l*PEI nanoparticles within one hour. The resulting nanoparticle suspension can be subjected to an optimized lyophilization protocol for storage in a powder form (Fig. 7A) that includes 9.5% w/w trehalose as a cryoprotectant agent. Lyophilized *p*DNA/*l*PEI nanoparticles were stable for at least 9 months when stored at −20°C. Upon reconstitution, the size, PDI, zeta-potential, PEI recovery, and DNA recovery at each time point were consistent with the freshly prepared sample (Fig. 7B). Reconstitution requires only the addition of water, free of aggressive processing such as sonication or vortexing. A clear suspension free of aggregation is generated after less than 1 minute at room temperature (Fig. 7A and Video S3). No vortexing is required. The reconstituted *p*DNA/*l*PEI nanoparticles are stable at 4°C for at least 4 days.

CONCLUSIONS

In this study, we combined a simulation method and an experimental approach to achieve a detailed understanding of the kinetics of mixing in the CIJ microchamber used for FNC assembly of *p*DNA/*l*PEI nanoparticles. The CIJ microchamber allows us to correlate the flow rates of the input *p*DNA and *l*PEI solutions with the characteristic mixing time of the mixing process. By controlling the mixing kinetics that enables the turbulent mixing of the solutions in the microchamber, we have demonstrated an explicit control over the nanoparticle size, surface charge and composition with high uniformity and scalability. We have used the static light scattering measurements and composition analysis of the FNC-assembled *p*DNA/*l*PEI nanoparticles, to reveal a "universal" correlation between the nanoparticle hydrodynamic size and *p*DNA payload per nanoparticle. This suggests that *p*DNA neutralization and compaction were achieved to the same degree for nanoparticles assembled with different *p*DNA payloads under different conditions. These findings not only allowed for finer composition control of *p*DNA/*l*PEI nanoparticles beyond control over nanoparticle size, but also provided experimental evidence to probe the kinetic process of *p*DNA/*l*PEI nanoparticle assembly. We confirmed that the charge neutralization between *p*DNA and *l*PEI molecules in forming PEC units is not a rate-limiting step, and the characteristic assembly time is primarily determined by chain folding and compaction of the PEC units. The number of *p*DNA packaged into each nanoparticle is primarily determined by the average diffusion distance of PEC units (*i.e.* the local *p*DNA concentration). By controlling the input *p*DNA concentration from 50 to 800 µg/mL under kinetically controlled conditions by FNC, an average of 1.3 to 21.8 *p*DNA can be assembled in to each nanoparticle, which correlates with the average hydrodynamic size of 35 to 130 nm.

The *p*DNA/*l*PEI nanoparticles with an N/P ratio of 3 to 6 can be produced with excellent shelf stability. These well-defined nanoparticles enabled the investigation of the effect of *p*DNA payload and formulation composition on their transfection efficiency. In both healthy and tumor bearing mouse models tested in this study, a payload of 6–10 plasmids per particle was found to be optimal for transgene expression in the lung following *i.v.* administration, which correlated well with their *in vitro* transfection activities.

These nanoparticles can be produced in a scalable manner as an off-the-shelf, lyophilized formulation that maintains its stability for at least 9 months when stored at −20 °C. Moreover, this formulation is easy to reconstitute and administer. Since this method is not specifically dependent on the carrier structure or on plasmid length and type, it should be generally applicable to many other potential polycation carriers. Thus, this FNC production process offers distinct technical advantages towards the clinical translation of non-viral nanoparticle vehicles for gene delivery.

EXPERIMENTAL SECTION

Simulation of turbulent mixing in the confined impinging jet (CIJ) micromixer.

Basic assumptions for simulation include: (1) Due to the low volume fraction of pDNA and PEI molecules in the flow, their presences do not affect the flow field; (2) Upon PEC formation, the kinematic viscosity of the efflux is close to water as the major viscosity contributor pDNA is already turned into a condensed form. Simulations are performed by solving the incompressible Navier-Stokes equations:

$$\nabla \cdot \overrightarrow{u} = 0 \tag{7}$$

$$\frac{\partial \overrightarrow{u}}{\partial t} + \nabla \cdot (\overrightarrow{u}\,\overrightarrow{u}) = -\frac{\nabla p}{\rho} + \upsilon \nabla^2 \overrightarrow{u} \tag{8}$$

where $\overrightarrow{u} = (u, v, w)$ is the fluid velocity vector, p is the pressure, p and p are the density and kinematic viscosity of water, respectively. They are solved by a fractional step method:

$$\frac{u_i^* - u_i^n}{\Delta t} + \frac{1}{2}\big[N_i^* + N_i^n\big] = -\frac{\delta p^n}{\delta x_i} + \frac{1}{2}\big[D_i^* + D_i^n\big] \tag{9}$$

$$\frac{u_i^{n+1} - u_i^*}{\Delta t} = -\frac{\delta p'}{\delta x_i} \tag{10}$$

where $N_i^n = \frac{\delta\big(U_i^n u_i^n\big)}{\delta x_i}$ and $D_i^n = \upsilon \frac{\partial^2 u_i}{\partial x_i^2}$. A second order Crank-Nicolson method is used for the time discretization of convection and diffusion terms, and a second order central finite difference method is used for spatial discretization. A sharp-interface immersed boundary method is used to resolve the geometry on the non-body conformal Cartesian grid.[24–25]

Preparations of pDNA/_in vivo_-jetPEI® polyelectrolyte complex (PEC) nanoparticles.

All CIJ devices were manufactured by Johns Hopkins University Whiting School of Engineering machine shop based on a CIJ design reported previously.[12] _In vivo_-jetPEI® (purchased from Polyplus-transfection, France) was used as received and diluted by ultrapure water to desired concentrations corresponding to different input N/P ratios from 3 to 6, when investigating the effect of input N/P ratio on nanoparticles with input pDNA concentration of 400 μg/mL. The pH of the solutions (regardless of the concentration) was

adjusted to 3.5 by 1 M NaOH or 1 M HCl solutions before use. The plasmids (Table S1, purchased from Aldevron, US or constructed by lab of Dr. Pomper) were diluted by ultrapure water to a concentration range from 50 to 800 μg/mL when investigating the effect of input *p*DNA concentration on nanoparticle assembly. The *p*DNA/*l*PEI nanoparticles were formulated by injecting the two working solutions into the CIJ chamber at the preset flow rates using a high-pressure syringe pump (New Era Pump Systems, US). The *p*DNA/*l*PEI nanoparticles were subjected to downstream characterizations and applications directly. When an isotonic condition is required, the *p*DNA and *l*PEI working solutions were prepared in 9.5% (w/w) trehalose instead of water. The nanoparticle formulations prepared by the FNC process were stable for at least one month in room temperature. For preparations of *p*DNA/*l*PEI nanoparticles (W9, Table 1) through pipetting, the procedure B3 was used as shown in Table S2.

Characterizations of the *p*DNA/*l*PEI nanoparticle preparations.

The *dynamic light scattering (DLS) measurements* were conducted using a Malvern ZEN3690 Zetasizer at 25°C to assess the z-average hydrodynamic diameter (D_z). We followed the definitions in DLS ISO 13321 to use the DLS size standard deviation to evaluate the uniformity of the nanoparticles with different D_z in Fig. 2A. Whenever there is a single peak for the nanoparticles measured, the DLS size standard deviation is directly related to the polydispersity index (PDI) and D_z that:

$$\text{DLS size standard deviation} = (D_Z{}^2 \times PDI)^{\frac{1}{2}} \quad\quad (11)$$

The *zeta-potential measurements* were conducted on the same Zetasizer by phase analysis light scattering (PALS) in a low-salt buffer (5 mM NaCl with a conductivity of 0.6 mS/cm) for all nanoparticle suspensions to improve the reliability of the measurements.

The *static light scattering (SLS) measurements* were conducted on a Wyatt DAWN HELEOS 18-angle laser light scattering photometer, equipped with a laser source with the wavelength of 658 nm and a fused silica flow cell as the optical compartment. The machine was calibrated with all the laser detectors normalized against an isotropic scatter (3 nm dextran, MW 9000–11000, Sigma, US). The *p*DNA/*l*PEI nanoparticle suspensions were diluted to appropriate concentrations and introduced into the flow cell through a filter with size cut-off of either 450 nm or 1000 nm. Each sample was run at a flow rate of 200 μL/min for 5 min to establish stable signals from the detectors. Data collection was followed for 5 min to give time-averaged intensities of each detector. The *p*DNA/*l*PEI nanoparticle suspensions exiting the flow cell were collected and subjected to DLS and DNA recovery assessments (Fig. S4) to confirm no loss of nanoparticles in the flow cells. The Zimm or Debye plots of the nanoparticles were generated using the Wyatt ASTRA 6.1 software. Three independent runs were conducted for each sample.

In order to calculate the weight average molar mass of the nanoparticles from SLS measurements, the *p*DNA/*l*PEI nanoparticles were modeled as copolymers consisting of two components,[36] as directed by light scattering theories.[37] The radius of gyration assessment was calculated regardless of possible variations of the nanoparticle morphology if form

factors of the experiments largely fall below 1 (as examined in Table S3). To determine the refractive index increment (dn/dc) of the pDNA/lPEI nanoparticles, we followed the additive rule described previously:[35]

$$\left(\frac{dn}{dc}\right)_{\text{Nanoparticle}} = w_{p\text{DNA}}\left(\frac{dn}{dc}\right)_{p\text{DNA}} + w_{l\text{PEI}}\left(\frac{dn}{dc}\right)_{\text{PEI}} \qquad (12)$$

where $w_{p\text{DNA}}$ and w_{PEI} are the weight fraction of pDNA and lPEI complexed in nanoparticles, respectively. The dn/dc values are available by plugging in input pDNA concentrations and bound lPEI fraction from results of free lPEI measurements. Based on the proposed models for nanoparticle assembly, for each one of pDNA molecule, all the associated bound lPEI have a molar mass of:

$$M_{\text{Associated } l\text{PEI}} = \gamma \times \frac{c_m(l\text{PEI})}{c_m(p\text{DNA})} \times M_{p\text{DNA}} \qquad (13)$$

where γ is bound lPEI fraction given by the free lPEI assessment; $c_m(l\text{PEI})$ and $c_m(p\text{DNA})$ are input mass concentrations of lPEI and pDNA for each formulation, respectively; and $M_{p\text{DNA}}$ is the molecular weight of the pDNA used. The weight average pDNA copy number per nanoparticle can be calculated by:

$$\overline{N} = \frac{\overline{M}_{Nanoparticle}}{M_{\text{Associated } l\text{PEI}} + M_{p\text{DNA}}} \qquad (14)$$

where $\overline{M}_{Nanoparticle}$ is the weight average molar mass of the nanoparticles given by SLS.

Transmission electron microscopy (TEM).

Carbon-coated copper grids (Electron Microscopy Services, US) were subjected to plasma treatment (N_2 glow discharge) for 30 sec to render the surface hydrophilic. The pDNA/lPEI nanoparticle suspensions were then loaded on the grid and incubated for 20 min. Excess suspension was removed, and an aliquot of 10 μL of 2% (w/v) uranyl acetate solution was added and incubated for 1 min. After removing the solution, the grids were allowed to be dried under hood for 24 h before imaging on a transmission electron microscope (Tecnai 12 Twin, Field Electron and Ion Company) operated at 100 kV. All images were taken by a Megaview III wide-angle camera (EMSIS GmbH, Germany).

Measurement of free lPEI in nanoparticle suspension.

The method was adapted from a previous report.[29] A 500-μL aliquot of nanoparticle suspension was added into a Vivaspin 500 centrifugal concentrator (PES, MWCO of 100,000, Sartorius, Germany), and then centrifuged for 1 min at 7200 rpm. The filtrate was analyzed using the Protein Red Advanced Protein Assay (PRAPA, purchased from Cytoskeleton, US) accordingly to the manufacturer's protocol. Each assay was conducted in quadruplicate. The lPEI reacts with the assay solution to generate products that have absorbance at a wavelength of 590 nm, through which the lPEI concentrations can be calculated against a linear standard curve.

In vitro transfection activity.

PC3 cancer cells were seeded in 24-well plates with a density of 5×10^4 cells/well. After 24-h culture, the medium in each well was aspirated. An aliquot of 50-μL *p*DNA/*l*PEI nanoparticle suspension containing 3 μg *p*DNA was added into 500 μL fresh medium, vortexed for 20 sec to mix, and the whole mixture was added into each well. The cells were incubated with the *p*DNA/*l*PEI nanoparticles for 1 to 4 h. The cells were then washed by PBS twice and incubated in 0.5 mL of fresh medium/well for 24 h. Before analysis, medium was removed and 100 μL of reporter lysis buffer (Promega, US) was added to each well. The cells were then subjected to two freezing-thawing cycles, and the lysate was analyzed using a luciferase assay kit (Promega, US). Transgene expression level was normalized against the total protein amount obtained by a protein assay kit (Pierce BCA reagents, Thermo Scientific, US). Pure luciferase was used as a standard. The transfection efficiency was plotted in terms of the amount of luciferase (ng) expressed per mg of total protein in the lysate. Transfection and analysis were conducted in quadruplicate for each group tested.

In vivo transfection efficiency.

The *in vivo* experimental procedures were approved by the Johns Hopkins Institutional Animal Care and Use Committee. The *p*DNA/*l*PEI nanoparticles were injected intravenously (*i.v.*) via mouse lateral tail vein at a dose of 30 or 40 μg *p*DNA per mouse at a concentration of 200 μg *p*DNA/mL. For groups with a lower input *p*DNA concentration in preparation, the nanoparticle suspensions were concentrated to 200 μg *p*DNA/mL by Amicon Ultra-2 centrifugal filter unit with a MWCO of 3,000 to concentrate both the PECs and the free PEI molecules with the same ratio. *In vivo* bioluminescence imaging was performed using the IVIS® Spectrum (PerkinElmer, US) and the images were processed with Living Image Software (PerkinElmer, US). The region of interest (ROI) quantitative analysis results have good correlations with luciferase protein abundance found in lungs that presents a linear relationship (Fig. S9), so tissue homogenization was not widely adopted for monitoring the kinetics of the transgene activities. Preliminary tests revealed that the transgene expression level (luciferase concentration in healthy lung tissues or tumor cells in the lung) peaks at around 12 and 48–72 h post injection for healthy BALB/c mouse model (Jackson Laboratory, US) and LL/2 metastasis in NSG mouse model (Johns Hopkins University Animal Core), respectively. IVIS assessment time points were set accordingly, with the mice anesthetized by isoflurane and imaged by IVIS system upon *i.p.* injection of 100 μL of 30 mg/mL D-luciferin (Gold Biotechnology, US) solution and 5-min diffusion period. For LL/2 tumor model, inoculation was done through *i.v.* injection of 200 μL PBS solution containing 5×10^5 cancer cells, 7 days prior to *p*DNA/*l*PEI nanoparticle dosing.

Cellular uptake and biodistribution studies.

The ^{3}H-labeled PEC nanoparticles were prepared according to a previous report.[45] The *p*DNA was labeled by methylation using S-adenosyl-L[methyl-^{3}H]-methionine (^{3}H-SAM, purchased from PerkinElmer, US. Application of radioactive materials in this study was approved and monitored by the Johns Hopkins University Radiation Safety Office) as the source prior to nanoparticle preparations. This labeling technique does not affect the nanoparticle assembly process. The advantage of this labeling technique lies with the

capability of assessing absolute quantity of labeled pDNAs in biological samples through counting disintegration events per minute (DPM), thus ideal for cellular uptake and biodistribution analyses of these nanoparticles. Within a working range, DPM is linearly proportional to labeled pDNA quantity in the assay (Fig. S6). To label pDNAs, water, 10× NEB buffer (New England Biolabs, US), ^{3}H-SAM (PerkinElmer, US), pDNA (1 mg/mL) and M. Sssl enzyme (New England Biolabs, US) were added at a ratio of 12:2:2:1:1 (v/v) into a 50-mL tube. The solution was mixed well, incubated for reaction at 37 °C for 2 h and quenched by heating to 65 °C for > 30 min. The reaction mixture was diluted by EB buffer, with labeled pDNA purified using a QIAprep Spin Miniprep kit (Qiagen, US), and finally mixed with nonlabelled pDNA to give the working solution for pDNA/lPEI nanoparticle assembly. For cellular uptake experiments, the same dose of pDNA/lPEI nanoparticles were used as that in the *in vitro* transfection experiment described above. At each time point, cells were washed twice with PBS and harvested. For the biodistribution study, the same dosage and formulation concentration were applied using the same protocol as described above for *in vivo* transfection experiments. At 1-h post injection, the animals were sacrificed with tissues harvested and weighed. Sufficient SOLVABLE solubilization fluid (PerkinElmer, US) was added to tissues and incubate at 70 °C for 48 h. The tissue lysate was mixed well, and 100 μL of each sample ($n = 3$ independent measurements) was added into 4 mL of Ultima Gold scintillation cocktail fluid (PerkinElmer, US) in 7-mL scintillation vials. DPM was assessed by a Tri-Carb 2200CA liquid scintillation analyzer (Packard Instrument Company, US) in a measurement time course of 5 min.

Supplementary Material

Refer to Web version on PubMed Central for supplementary material.

ACKNOWLEDGEMENTS

REFERENCES

(1). Shi B; Zheng M; Tao W; Chung R; Jin D; Ghaffari D; Farokhzad OC Challenges in DNA Delivery and Recent Advances in Multifunctional Polymeric DNA Delivery Systems. Biomacromolecules 2017, 18, 2231–2246. [PubMed: 28661127]

(2). Hickey JW; Santos JL; Williford J-M; Mao H-Q Control of Polymeric Nanoparticle Size to Improve Therapeutic Delivery. J. Controlled Release 2015, 219, 536–547.

(3). Williford J-M; Santos JL; Shyam R; Mao H-Q Shape Control in Engineering of Polymeric Nanoparticles for Therapeutic Delivery. Biomater. Sci 2015, 3, 894–907. [PubMed: 26146550]

(4). Blanco E; Shen H; Ferrari M Principles of Nanoparticle Design for Overcoming Biological Barriers to Drug Delivery. Nat. Biotechnol 2015, 33, 941. [PubMed: 26348965]

(5). Lu M; Ho Y-P; Grigsby CL; Nawaz AA; Leong KW; Huang TJ Three-Dimensional Hydrodynamic Focusing Method for Polyplex Synthesis. ACS Nano 2014, 8, 332–339. [PubMed: 24341632]

(6). Lu M; Ozcelik A; Grigsby CL; Zhao Y; Guo F; Leong KW; Huang TJ Microfluidic Hydrodynamic Focusing for Synthesis of Nanomaterials. Nano Today 2016, 11, 778–792. [PubMed: 30337950]

(7). Juul S; Nielsen CJF; Labouriau R; Roy A; Tesauro C; Jensen PW; Harmsen C; Kristoffersen EL; Chiu Y-L; Frøhlich R; Fiorani P; Cox-Singh J; Tordrup D; Koch J; Bienvenu A-L; Desideri A; Picot S; Petersen E; Leong KW; Ho Y-P; Stougaard M; Knudsen BR Droplet Microfluidics Platform for Highly Sensitive and Quantitative Detection of Malaria-Causing Plasmodium Parasites Based on Enzyme Activity Measurement. ACS Nano 2012, 6, 10676–10683. [PubMed: 23121492]

(8). Kasper JC; Schaffert D; Ogris M; Wagner E; Friess W The Establishment of An Up-scaled Micro-mixer Method Allows the Standardized and Reproducible Preparation of Well-defined Plasmid/LPEI Polyplexes. Eur. J. Pharm. Biopharm 2011, 77, 182–185. [PubMed: 21094683]

(9). Feng Q; Sun J; Jiang X Microfluidics-mediated Assembly of Functional Nanoparticles for Cancer-related Pharmaceutical Applications. Nanoscale 2016, 8, 12430–12443. [PubMed: 26864887]

(10). Liu D; Cito S; Zhang Y; Wang C-F; Sikanen TM; Santos HA A Versatile and Robust Microfluidic Platform Toward High Throughput Synthesis of Homogeneous Nanoparticles with Tunable Properties. Adv. Mater 2015, 27, 2298–2304. [PubMed: 25684077]

(11). Liu D; Zhang H; Cito S; Fan J; Mäkilä E; Salonen J; Hirvonen J; Sikanen TM; Weitz DA; Santos HA Core/Shell Nanocomposites Produced by Superfast Sequential Microfluidic Nanoprecipitation. Nano Lett. 2017, 17, 606–614. [PubMed: 28060521]

(12). Johnson BK; Prud'homme RK Chemical Processing and Micromixing in Confined Impinging Jets. AIChE J. 2003, 49, 2264–2282.

(13). Liu Y; Fox RO CFD Predictions for Chemical Processing in A Confined Impinging-jets Reactor. AIChE J. 2006, 52, 731–744.

(14). Liu Y; Cheng C; Liu Y; Prud'homme RK; Fox RO Mixing in A Multi-inlet Vortex Mixer (MIVM) for Flash Nano-precipitation. Chem. Eng. Sci 2008, 63, 2829–2842.

(15). He Z; Santos JL; Tian H; Huang H; Hu Y; Liu L; Leong KW; Chen Y; Mao H-Q Scalable Fabrication of Size-controlled Chitosan Nanoparticles for Oral Delivery of Insulin. Biomaterials 2017, 130, 28–41. [PubMed: 28359018]

(16). He Z; Hu Y; Nie T; Tang H; Zhu J; Chen K; Liu L; Leong KW; Chen Y; Mao H-Q Size-controlled Lipid Nanoparticle Production Using Turbulent Mixing to Enhance Oral DNA Delivery. Acta Biomater. 2018, 81, 195–207. [PubMed: 30267888]

(17). Santos JL; Ren Y; Vandermark J; Archang MM; Williford J-M; Liu H-W; Lee J; Wang T-H; Mao H-Q Continuous Production of Discrete Plasmid DNA-Polycation Nanoparticles Using Flash Nanocomplexation. Small 2016, 12, 6214–6222. [PubMed: 27717227]

(18). Saad WS; Prud'homme RK Principles of Nanoparticle Formation by Flash Nanoprecipitation. Nano Today 2016, 11, 212–227.

(19). Nikoubashman A; Lee VE; Sosa C; Prud'homme RK; Priestley RD; Panagiotopoulos AZ Directed Assembly of Soft Colloids through Rapid Solvent Exchange. ACS Nano 2016, 10, 1425–1433. [PubMed: 26692293]

(20). Zhang C; Pansare VJ; Prud'homme RK; Priestley RD Flash Nanoprecipitation of Polystyrene Nanoparticles. Soft Matter 2012, 8, 86–93.

(21). Johnson BK; Prud'homme RK Mechanism for Rapid Self-Assembly of Block Copolymer Nanoparticles. Phys. Rev. Lett 2003, 91, 118302. [PubMed: 14525460]

(22). Pagels RF; Edelstein J; Tang C; Prud'homme RK Controlling and Predicting Nanoparticle Formation by Block Copolymer Directed Rapid Precipitations. Nano Lett. 2018, 18, 1139–1144. [PubMed: 29297690]

(23). A First Course in Turbulence; Tennekes H; Lumley JL; Lumley J; MIT Press: Massachusetts, 1972.

(24). Mittal R; Dong H; Bozkurttas M; Najjar FM; Vargas A; von Loebbecke A A Versatile Sharp Interface Immersed Boundary Method for Incompressible Flows with Complex Boundaries. J. Comput. Phys 2008, 227, 4825–4852. [PubMed: 20216919]

(25). Seo JH; Mittal R A Sharp-interface Immersed Boundary Method with Improved Mass Conservation and Reduced Spurious Pressure Oscillations. J. Comput. Phys 2011, 230, 7347–7363. [PubMed: 21857745]

(26). Clamme JP; Azoulay J; Mely Y Monitoring of the Formation and Dissociation of Polyethylenimine/DNA Complexes by Two Photon Fluorescence Correction Spectroscopy. Biophys. J 2003, 84, 1960–1968. [PubMed: 12609898]

(27). Curtis KA; Miller D; Millard P; Basu S; Horkay F; Chandran PL Unusual Salt and pH Induced Changes in Polyethylenimine Solutions. PLoS One 2016, 11, e0158147. [PubMed: 27685846]

(28). Yue Y; Jin F; Deng R; Cai J; Chen Y; Lin MCM; Kung H-F; Wu C Revisit Complexation between DNA and Polyethylenimine — Effect of Uncomplexed Chains Free in the Solution Mixture on Gene Transfection. J. Controlled Release 2011, 155, 67–76.

(29). Bertschinger M; Chaboche S; Jordan M; Wurm FM A Spectrophotometric Assay for the Quantification of Polyethylenimine in DNA Nanoparticles. Anal. Biochem 2004, 334, 196–198. [PubMed: 15464969]

(30). Berret J-F Evidence of Overcharging in the Complexation between Oppositely Charged Polymers and Surfactants. J. Chem. Phys 2005, 123, 164703. [PubMed: 16268718]

(31). Barreleiro PCA; Lindman B The Kinetics of DNA–Cationic Vesicle Complex Formation. J. Phys. Chem. B 2003, 107, 6208–6213.

(32). Santhiya D; Dias RS; Dutta S; Das PK; Miguel MG; Lindman B; Maiti S Kinetic Studies of Amino Acid-Based Surfactant Binding to DNA. J. Phys. Chem. B 2012, 116, 5831–5837. [PubMed: 22554103]

(33). Osada K; Shiotani T; Tockary TA; Kobayashi D; Oshima H; Ikeda S; Christie RJ; Itaka K; Kataoka K Enhanced Gene Expression Promoted by the Quantized Folding of pDNA within Polyplex Micelles. Biomaterials 2012, 33, 325–332. [PubMed: 21993237]

(34). Takeda KM; Osada K; Tockary TA; Dirisala A; Chen Q; Kataoka K Poly(ethylene glycol) Crowding as Critical Factor To Determine pDNA Packaging Scheme into Polyplex Micelles for Enhanced Gene Expression. Biomacromolecules 2017, 18, 36–43. [PubMed: 27990798]

(35). Dai Z; Wu C How Does DNA Complex with Polyethylenimine with Different Chain Lengths and Topologies in Their Aqueous Solution Mixtures? Macromolecules 2012, 45, 4346–4353.

(36). Dautzenberg H; Koetz J; Linow KJ; Philipp B; Rother G Static Light Scattering of Polyelectrolyte Complex Solutions In Macromolecular complexes in chemistry and biology; Dubin P, Bock J, Davis R, Schulz DN, Thies C, Eds.; Springer Science & Business Media: Berlin, 2012; pp 119–133.

(37). Light Scattering by Polymer Solutions In Polymer chemistry; Hiemenz PC; Lodge TP; CRC Press Taylor and Francis: New York, 2007; pp 289–325.

(38). Boeckle S; von Gersdorff K; van der Piepen S; Culmsee C; Wagner E; Ogris M Purification of polyethylenimine polyplexes highlights the role of free polycations in gene transfer. J. Gene Med 2004, 6, 1102–1111. [PubMed: 15386739]

(39). Tsoi KM; MacParland SA; Ma X-Z; Spetzler VN; Echeverri J; Ouyang B; Fadel SM; Sykes EA; Goldaracena N; Kaths JM; Conneely JB; Alman BA; Selzner M; Ostrowski MA; Adeyi OA; Zilman A; McGilvray ID; Chan WCW Mechanism of Hard-nanomaterial Clearance by the Liver. Nat. Mater 2016, 15, 1212. [PubMed: 27525571]

(40). Ogris M; Brunner S; Schüller S; Kircheis R; Wagner E PEGylated DNA/transferrin-PEI Complexes: Reduced Interaction with Blood Components, Extended Circulation in Blood and Potential for Systemic Gene Delivery. Gene Ther. 1999, 6, 595. [PubMed: 10476219]

(41). Klauber TCB; Søndergaard RV; Sawant RR; Torchilin VP; Andresen TL Elucidating the Role of Free Polycations in Gene Knockdown by siRNA Polyplexes. Acta Biomater. 2016, 35, 248–259. [PubMed: 26884277]

(42). Bhang H-EC; Gabrielson KL; Laterra J; Fisher PB; Pomper MG Tumor-specific Imaging through Progression Elevated Gene-3 Promoter-driven Gene Expression. Nat. Med 2010, 17, 123. [PubMed: 21151140]

(43). Minn I; Bar-Shir A; Yarlagadda K; Bulte JWM; Fisher PB; Wang H; Gilad AA; Pomper MG Tumor-specific Expression and Detection of A CEST Reporter Gene. Magn. Reson. Med 2015, 74, 544–549. [PubMed: 25919119]

(44). Bertram JS; Janik P Establishment of A Cloned Line of Lewis Lung Carcinoma Cells Adapted to Cell Culture. Cancer Lett. 1980, 11, 63–73. [PubMed: 7226139]
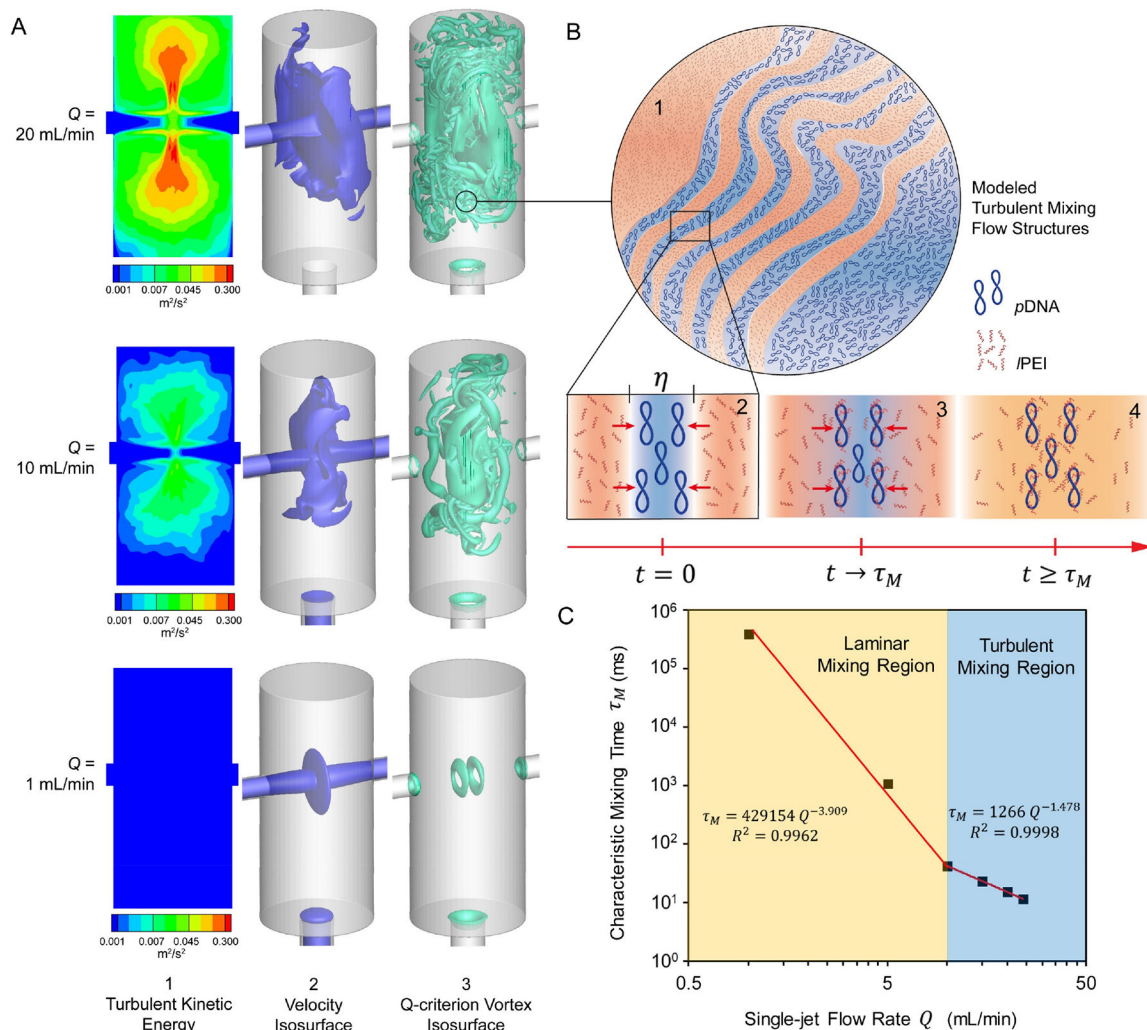
(45). Williford J-M; Archang MM; Minn I; Ren Y; Wo M; Vandermark J; Fisher PB; Pomper MG Critical Length of PEG Grafts on lPEI/DNA Nanoparticles for Efficient in Vivo Delivery. ACS Biomater. Sci. Eng 2016, 2, 567–578. [PubMed: 27088129]

Figure 1. Turbulent mixing of *p*DNA and *l*PEI solutions in a confined impinging jet (CIJ) microchamber.

(A) Simulated flow fields based on the actual CIJ mixer dimensions: (1) Time-averaged turbulent kinetic energy (TKE) distribution, (2) Instantaneous velocity isosurface sampled at $t = 110$ ms, and (3) Instantaneous Q-criterion vortex isosurface sampled at $t = 110$ ms; **(B)** Illustrations of (1) the *turbulent mixing flow structures* generated at a flow rate of 20 mL/min, (2) separation of the *p*DNA and *l*PEI solution flows at the Kolmogorov length scale η, (3) diffusion of *l*PEI molecules into the *p*DNA flow regions, and (4) uniform mixing as defined by the input concentration profile of *p*DNA and *l*PEI across a time scale of τ_M; **(C)** Correlation between the characteristic mixing time τ_M and flow rate Q, as fitted from simulation results of 6 different flow rates.
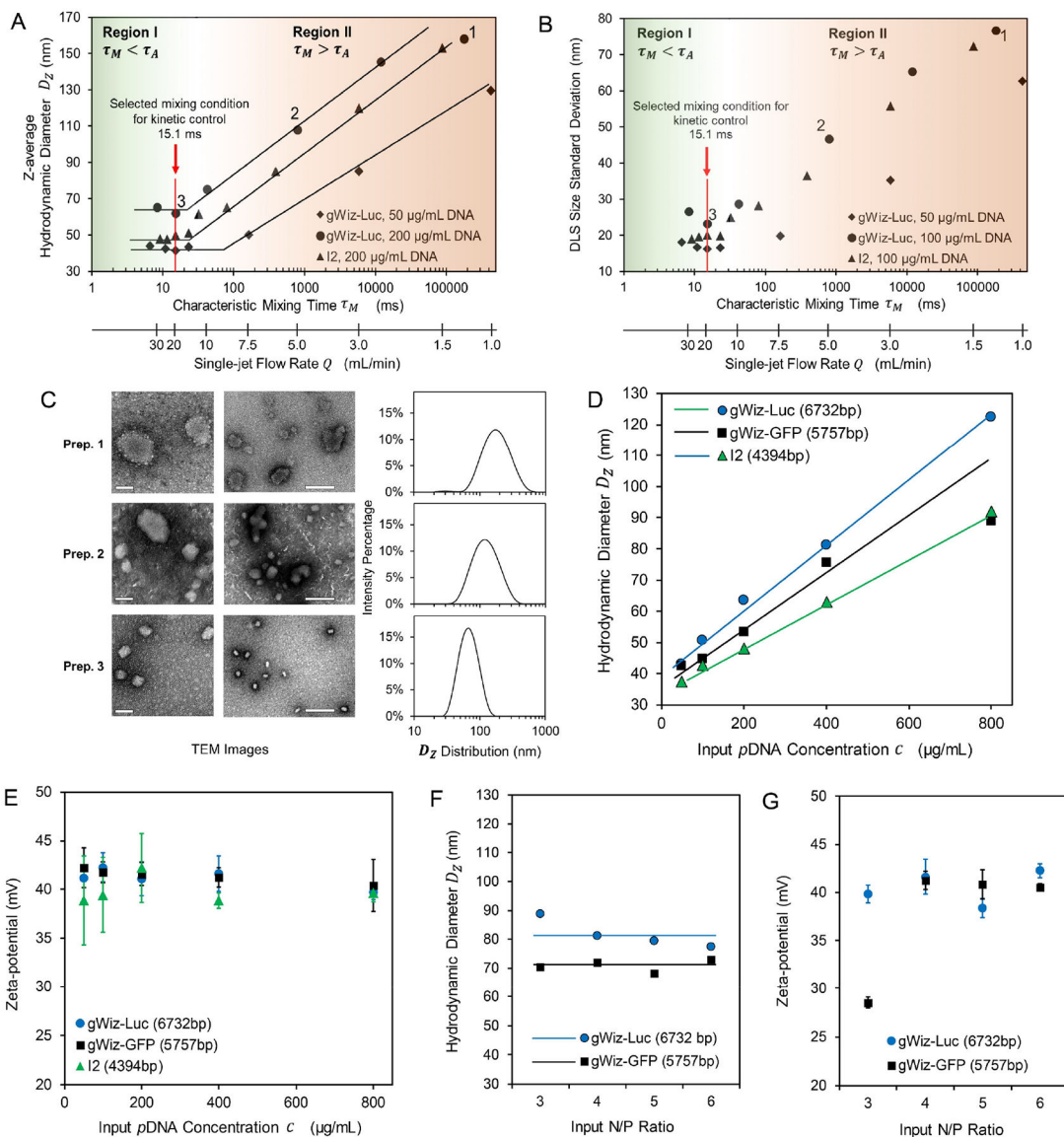
Figure 2. Effect of characteristic mixing time τ_M on pDNA/lPEI nanoparticle assembly.
(A, B) Effect of mixing kinetics profile (τ_M and flow rate Q) on the average nanoparticle size D_Z (A) and uniformity shown as the DLS size standard deviation (B). The mixing kinetics scale is divided into two regions: Region I ($\tau_M < \tau_A$) and Region II ($\tau_M > \tau_A$). Labels 1, 2 and 3 denote three representative preparations generated from three different mixing conditions; **(C)** Transmission electron microscopy (TEM) images and DLS profiles of the three sets of nanoparticles prepared at $Q = 1.25$ mL/min, $\tau_M = 1.8 \times 10^5$ ms (Prep. 1), $Q = 5$ mL/min, $\tau_M = 790$ ms (Prep. 2), and $Q = 20$ mL/min, $\tau_M = 15$ ms (Prep. 3). Scale bar = 50 nm (for left panel) and 200 nm (for right panel); **(D, E)** Effect of input pDNA concentration and plasmid size on the average nanoparticle size D_Z (D) and zeta potential (E) prepared by $\tau_M = 15$ ms; **(F, G)** Effect of N/P ratio on the average nanoparticle size D_Z (F) and zeta potential (G) prepared by $\tau_M = 15$ ms. For the conditions tested, the size profile and zeta potential of pDNA/lPEI nanoparticles did not vary with the N/P ratio from 4 to 6.
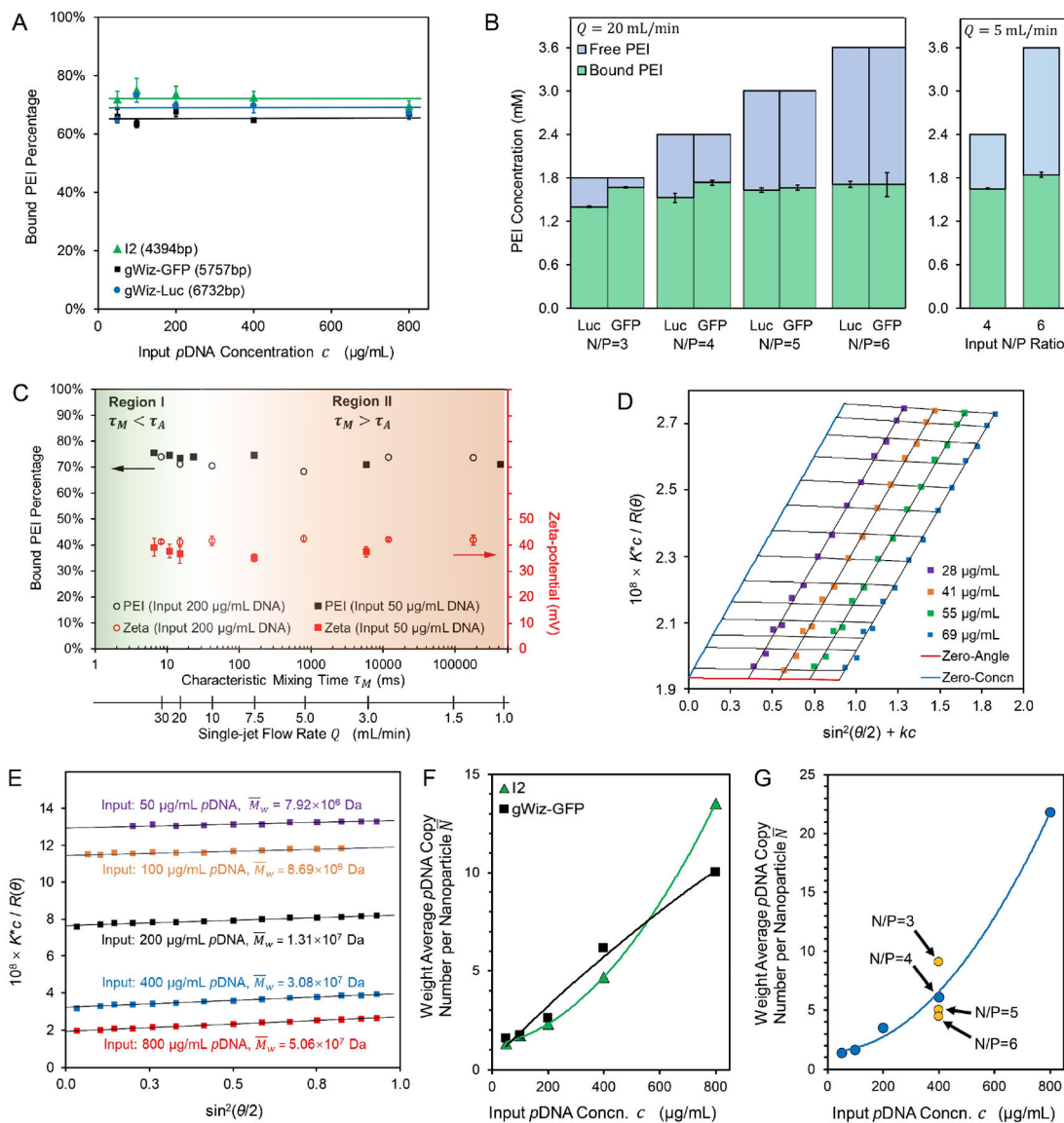
Figure 3. Compositions of the FNC-assembled _p_DNA//_l_PEI nanoparticles.
(A) The fraction of bound _l_PEI and the composition of the assembled nanoparticles remained similar when nanoparticles were prepared at different input _p_DNA concentrations or with different plasmids; **(B)** Bound _vs._ free _l_PEI amount and proportions with an input N/P ratio from 3 to 6 for gWiz-Luc and gWiz-GFP nanoparticle formulations assembled under a turbulent mixing condition ($Q = 20$ mL/min, $\tau_M = 15$ ms $< \tau_A$) and a laminar mixing condition ($Q = 5$ mL/min, $\tau_M = 790$ ms $> \tau_A$). Labels: Luc and GFP for gWiz-Luc and gWiz-GFP plasmid nanoparticles, respectively; **(C)** Bound _l_PEI fraction and zeta-potential of nanoparticles prepared with 50 or 200 μg/mL of gWiz-Luc _p_DNA under different flow rates, suggesting that all gWiz-Luc/_l_PEI nanoparticles share the same average composition; **(D)** A representative Zimm plot for I2/_l_PEI nanoparticles with a molar mass of 5.32×10^7 Da, also showing the second viral coefficient A approaching zero; **(E)** Representative Debye plots for gWiz-GFP/_l_PEI nanoparticles prepared by varying input _p_DNA concentration for I2
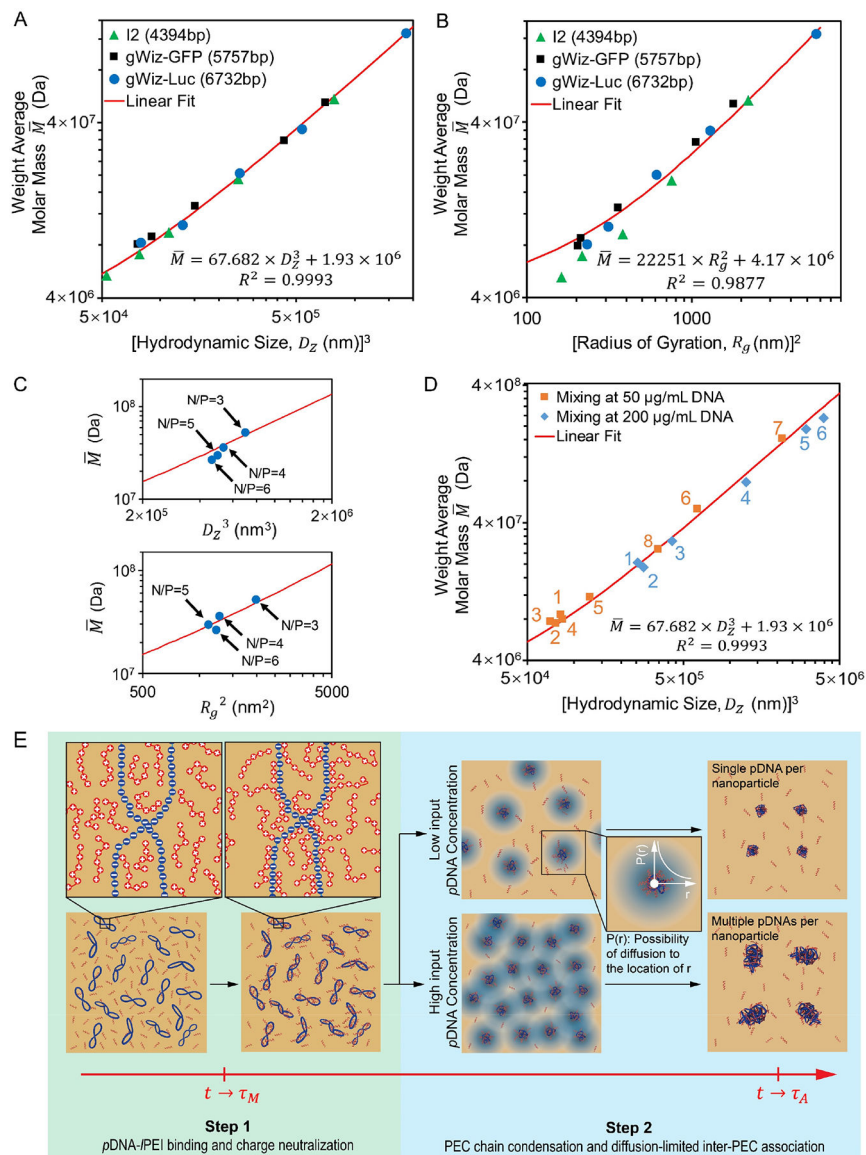
plasmid; **(F, G)** Calculated weight average pDNA copy numbers per nanoparticle (N) for preparations from lPEI and I2 or gWiz-GFP plasmids at N/P = 4 (F) or gWiz-Luc plasmid at different concentrations and N/P ratios (G).

Figure 4. Assembly of *p*DNA/*l*PEI PEC nanoparticles.

(A, B) Correlation of nanoparticle average molar mass and size (A) and radius of gyration (B) for nanoparticles assembled under turbulent mixing condition (Q = 20 mL/min, τ_M = 15 ms). Each data point in (A) and (B) represents an independent formulation batch; **(C)** Application of the linear fits from Eq. 5 (Upper panel) and Eq. 6 (Bottom panel) to nanoparticles formulated with different N/P ratios at Q = 20 mL/min; **(D)** Correlation of nanoparticle average molar mass and size for nanoparticles produced by different mixing conditions, *i.e.* with different τ_M. For input *p*DNA concentration of 25 μg/mL (orange), label 1 to 8 represent τ_M of 7, 11, 15, 23, 163, 5855, 4×10^5 ms, and pipetting respectively; for 100 μg/mL (blue), label 1 to 6 represent τ_M of 8, 15, 42, 795, 10^4 and 2×10^5 ms, respectively; **(E)** The proposed two-step *p*DNA/*l*PEI PEC nanoparticle assembly model under turbulent mixing condition ($\tau_M < \tau_A$).
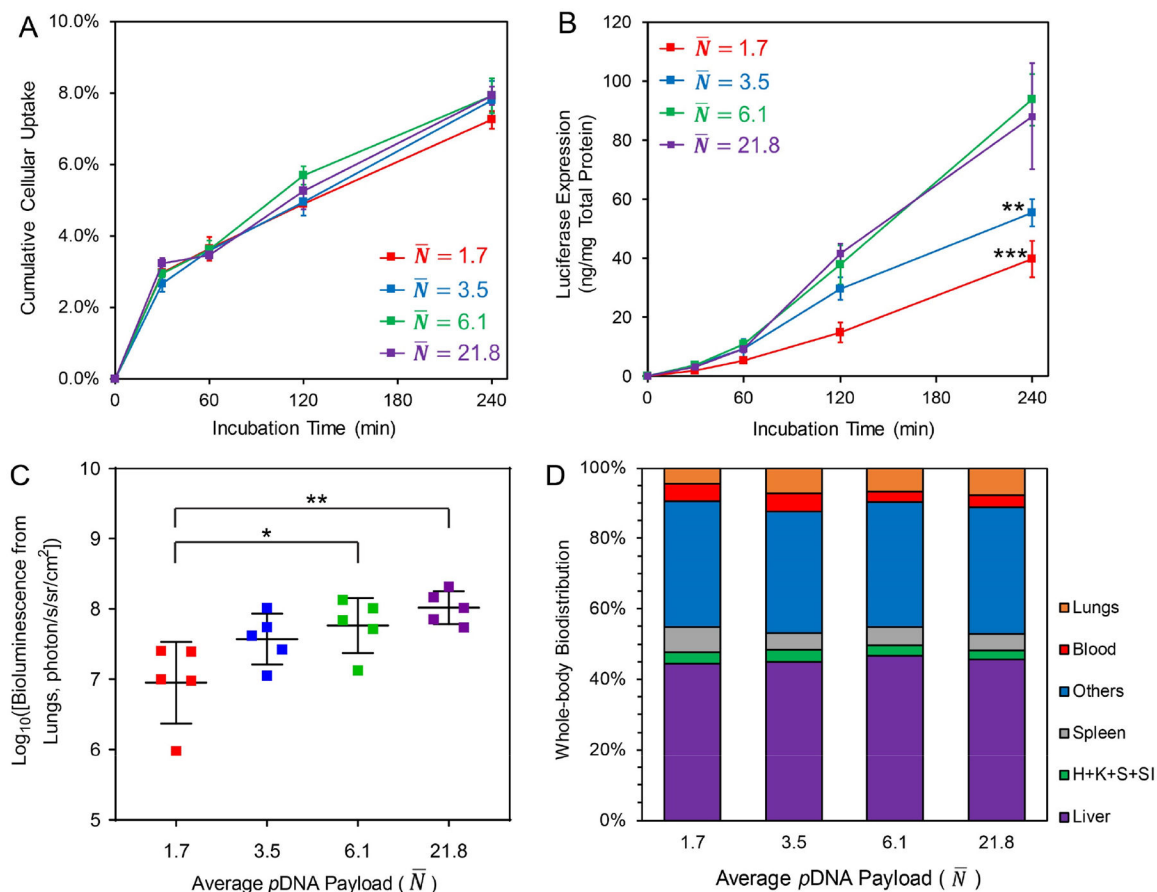
Figure 5. Transfection process and efficiency of *p*DNA//*l*PEI nanoparticles with different numbers of *p*DNA per particle.
(A) Cellular uptake quantitative assay of nanoparticles prepared with ^{3}H-labeled *p*DNA in PC3 prostate cell line following a 4-h incubation period (*p*DNA dosage = 0.6 μg/10^4 cells); **(B)** The *in vitro* transfection efficiency of nanoparticles with different $\overline{N}$ in PC3 cells with a 4-h incubation (*p*DNA dosage = 0.6 μg/10^4 cells). The asterisks denote significance level when comparing with $\overline{N}$ = 6.1 nanoparticle group; **(C)** The *in vivo* transfection efficiency (bioluminescence radiance) in the lung of BALB/c mice at 12 h post *i.v.* injection of nanoparticles (dose = 30 μg *p*DNA per mouse); **(D)** Whole-body biodistribution of nanoparticles at 1-h post *i.v.* injection of ^{3}H-labeled nanoparticles containing 30 μg *p*DNA per mouse. Labels: H: heart, K: kidneys, S: stomach, SI: small intestine. For statistical analysis, *p < 0.05, **p < 0.01, and ***p < 0.001 from one-way ANOVA and multiple comparisons (GraphPad Prism 8).
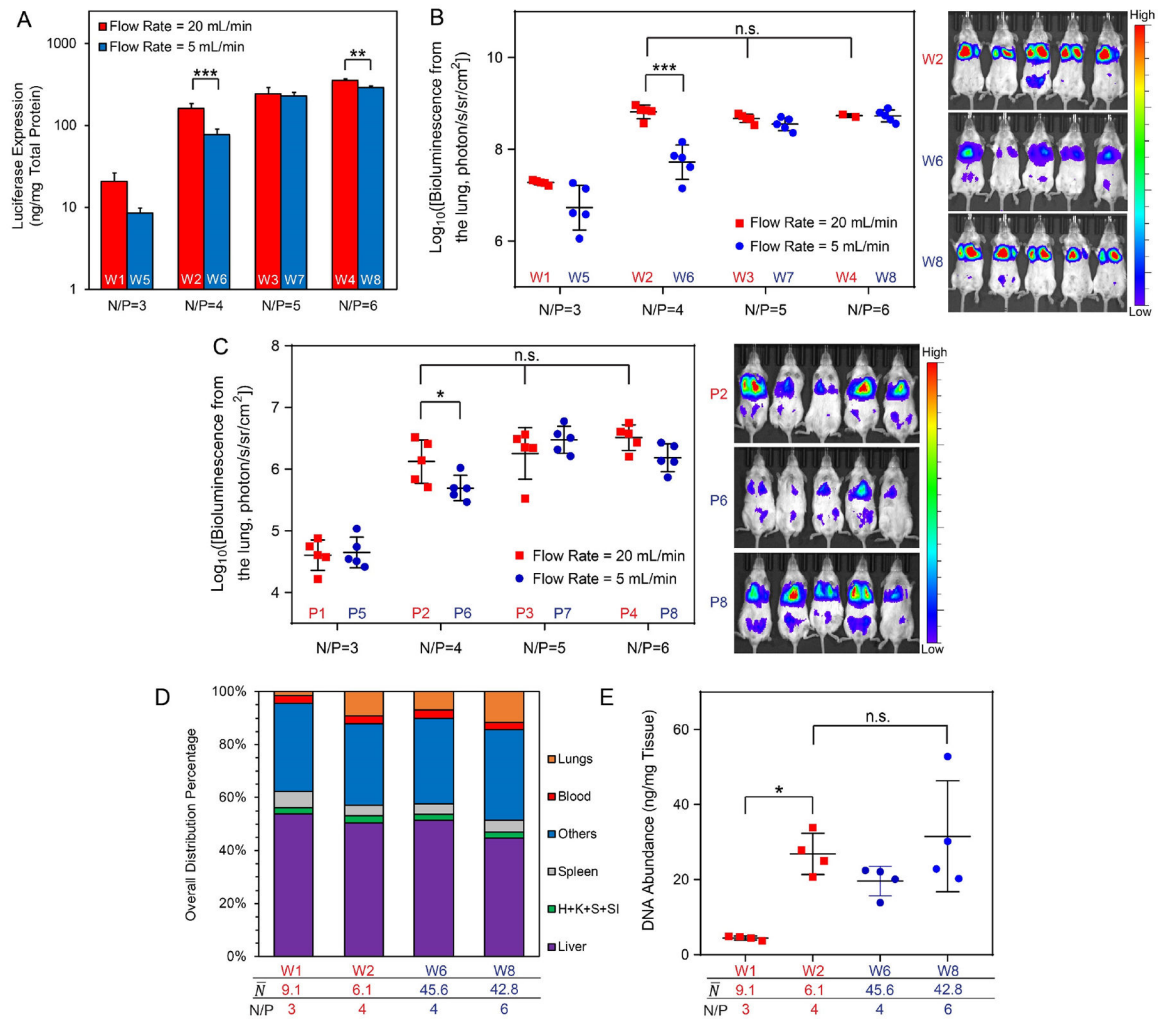
Figure 6. Transgene expression of *p*DNA//PEI nanoparticles produced under kinetically controlled conditions with different N/P ratios and payload levels ($\overline{N}$).
(A) *In vitro* transfection efficiencies of nanoparticles (W1–W8, see Table 1) in PC3 cancer cell line (dose = 0.6 µg gWiz-Luc plasmid/10^4 cells); **(B)** *In vivo* transfection efficiency in the lung in healthy BALB/c mice at 12 h post *i.v.* injection of nanoparticles (W1–W8, see Table 1) containing 40 µg gWiz-Luc plasmid per mouse (left) and representative IVIS images of groups with significant differences in transgene expression (right); **(C)** *In vivo* transfection efficiency in the lung of an LL/2 metastasis model in the NSG mice at 48 h post injection of nanoparticles (P1-P8, see Table 1) containing 40 µg PEG-Luc plasmid per mouse (left) and representative IVIS images of groups with significant differences in transgene expression (right); **(D)** Whole-body biodistributions in BALB/c mice at 1 h post injection of nanoparticles (W1, W2, W6, W8) containing 40 µg ^{3}H-labeled gWiz-Luc plasmid per mouse. Labels: H: heart, K: kidneys, S: stomach, SI: small intestine; **(E)** Biodistributions to the lung of mice shown in (D); For statistical analysis, n.s. denotes no statistical significance with $p > 0.05$, *$p < 0.05$, **$p < 0.01$, and ***$p < 0.001$ from one-way or two-way ANOVA and multiple comparisons.
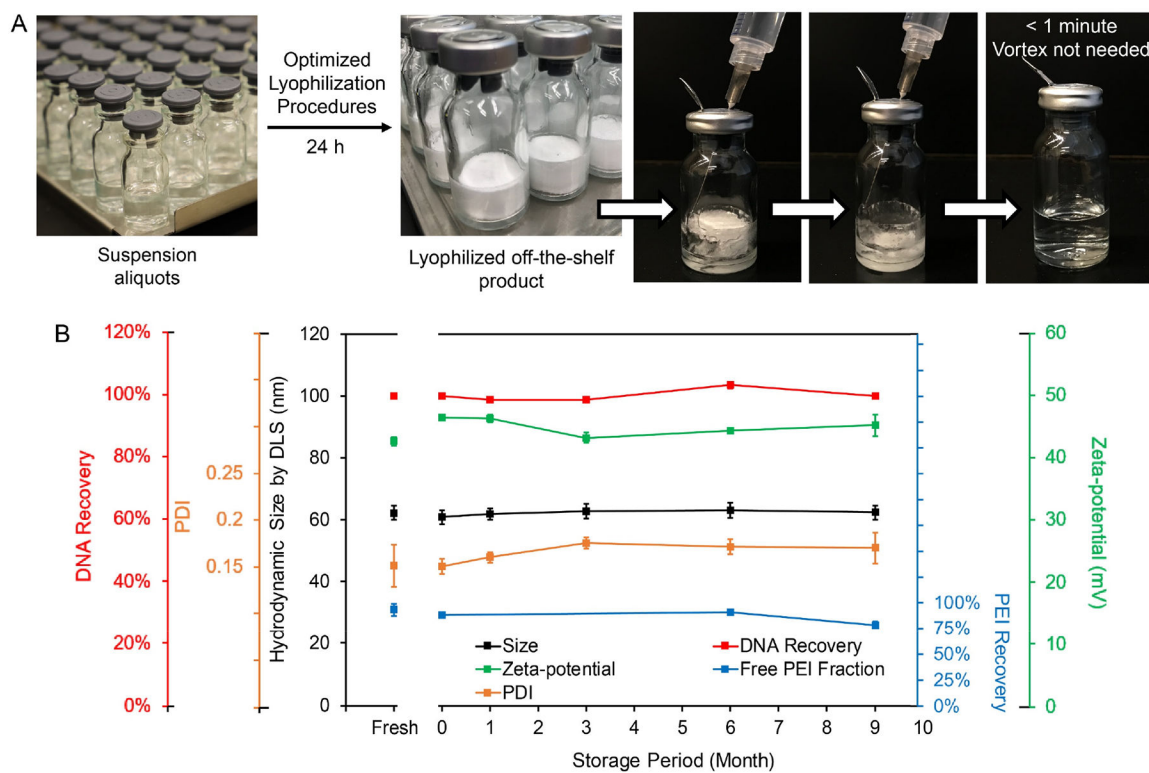
Figure 7. Scale-up production of off-the-shelf *p*DNA//PEI nanoparticles and the long-term storage stability.

(A) Lyophilization and reconstitution of nanoparticles prepared using FNC setup; **(B)** Nanoparticle characteristics upon reconstitution of lyophilized nanoparticles stored at −20°C at Months 0, 1, 3, 6 and 9. Month 0 represents a reconstituted sample right after completion of lyophilization.

Table 1.

pDNA/lPEI nanoparticles prepared with different mixing conditions and N/P ratios

Nanoparticle Code	Plasmid	Q (mL/min)	Input N/P	Z-average Diameter* D_z (nm)	Weight Average $\overline{N}$
W1			3	88.2 ± 30.0	9.1
W2			4	81.2 ± 25.5	6.1
W3		20	5	79.3 ± 40.4	5.0
W4			6	77.5 ± 30.1	4.4
W5	gWiz-Luc		3	153.0 ± 61.9	40.7**
W6			4	158.9 ± 64.5	45.6**
W7		5	5	148.1 ± 62.8	37.0**
W8			6	155.5 ± 72.0	42.8**
W9		Pipetting	6	171.2 ± 86.3	57.0**
P1			3	81.4 ± 21.2	8.1**
P2			4	86.0 ± 25.1	9.5**
P3		20	5	82.7 ± 28.4	8.5**
P4	PEG-fLuc		6	81.0 ± 26.6	8.0**
P5			3	146.9 ± 57.8	45.7**
P6			4	151.1 ± 60.2	49.7**
P7		5	5	145.6 ± 54.7	44.5**
P8			6	134.1 ± 46.6	34.9**

* Reported as Z-average hydrodynamic diameter ± DLS size standard deviation.

** Calculated based on Eqs. 5 and 14.